THE ASTROPHYSICAL JOURNAL, 463:444–465, 1996 June 1

ON THE SPECTRAL ENERGY DISTRIBUTIONS OF BLAZARS

RITA M. SAMBRUNA[1]
Space Telescope Science Institute, 3700 San Martin Drive, Baltimore, MD 21218
LAURA MARASCHI
Dipartimento di Fisica, Università Genova, via Dodecaneso 33, 16146 Genova, Italy
AND
C. MEGAN URRY
Space Telescope Science Institute, 3700 San Martin Drive, Baltimore, MD 21218
Received 1995 August 24; accepted 1995 December 6

ABSTRACT

We investigated the multifrequency spectral properties of complete samples of three different kinds of blazars, all observed with the *ROSAT* PSPC in pointed mode. These include the 1 Jy sample of radio-selected BL Lacs (RBLs), the *Einstein* Extended Medium Sensitivity Survey sample of X-ray–selected BL Lacs (XBLs), and a small but complete sample of flat spectrum radio quasars (FSRQs) from the S5 radio survey. We compared their spectral energy distributions from the radio through the X-ray bands using the *ROSAT* data and nonsimultaneous radio, infrared, and optical fluxes from the literature. The individual spectral energy distributions in the rest-frame log (νL_ν) versus log ν representation were fitted with a parabolic function, in order to estimate the bolometric luminosities and peak emission frequencies of each source. We find that the spectral energy distributions of the three kinds of blazars are different but essentially continuous: XBLs and FSRQs occupy separate regions in broadband color-color diagrams, while RBLs bridge the gap between the two populations. Describing the shape of the optical–to–X-ray continua with the composite spectral index $\alpha_{ox} - \alpha_x$, for which positive or negative values indicate concave or convex spectra, respectively, we find that the optical–to–X-ray continua tend to be convex for XBLs and concave for FSRQs, while the RBL sample contains objects with XBL-like and with FSRQ-like spectra. For the three samples combined, the spectral index connecting the radio and optical bands, α_{ro}, is strongly correlated with $\alpha_{ox} - \alpha_x$ and with the bolometric luminosity or redshift, in the sense that sources with steeper α_{ro} are more luminous (distant) and have concave optical–to–X-ray shapes. This shows that the continuum emission of blazars can be characterized by essentially one parameter and suggests that the spectral shape is fundamentally connected to the bolometric luminosity and/or redshift. We discuss the physical parameters deduced for the different blazar classes assuming relativistically beamed synchrotron and inverse-Compton radiation from a homogeneous emission region and from an inhomogeneous jet. We show that the observed sequence of spectral properties of blazars cannot be easily accounted for in terms of a sole change in viewing angle but requires instead a systematic change of instrinsic physical parameters, such as magnetic field, jet size, and maximum electron energy. The change is in the sense that XBLs have higher magnetic fields/electron energies and smaller sizes than radio-selected blazars.

Subject headings: BL Lacertae objects: general — quasars: general — radiation mechanisms: nonthermal — X-rays: galaxies

1. INTRODUCTION

Blazars are compact, flat spectrum radio sources with highly variable and polarized nonthermal continuum emission extending up to X-ray and often γ-ray frequencies. In some cases their emission lines are very weak or absent (equivalent width <5 Å), a property which defines the subclass of BL Lacertae objects. Other blazars have broad emission lines similar to those of normal quasars; depending on how they were identified, these are known as optically violently variable quasars, highly polarized quasars,[2] flat spectrum radio quasars (FSRQs), or core-dominant radio quasars.

The continuum emission in blazars is thought to arise from a relativistic jet oriented close to the observer, meaning it is highly beamed in the forward direction. Blazars thus represent a special orientation of some more mundane species, most likely radio galaxies (for a recent review of this unification scheme, see Urry & Padovani 1995). Strong evidence for relativistic motion of the emitting plasma is provided by the observation of superluminal expansion of radio knots relative to the radio core in numerous blazars (Vermeulen & Cohen 1994). The recent detection of several dozen blazars in high-energy γ-rays (Thompson et al. 1995; von Montigny et al. 1995) also suggests the high-energy emission is relativistically beamed, provided X-rays and γ-rays are cospatial (Dondi & Ghisellini 1995; Maraschi, Ghisellini, & Celotti 1992; but cf. Dermer & Gehrels 1995).

Most blazars have been found in high-frequency radio surveys, which favor the detection of such flat spectrum sources. Complete samples of BL Lac objects and FSRQs

[1] Presently NRC Research Associate at Goddard Space Flight Center, Code 662, Greenbelt, MD 20771 (sambruna@attilla.gsfc.nasa.gov).

[2] We refer here only to radio-loud HPQs. While a few radio-quiet quasars also have highly polarized optical emission, and thus fit the HPQ definition, their polarization is almost certainly caused by scattering rather than intrinsic emission processes.

have been derived from such radio catalogs (Stickel et al. 1991; Impey & Tapia 1988; Pearson & Readhead 1988; Wall & Peacock 1988). Blazars are also X-ray emitters (Giommi et al. 1987; Bierman et al. 1981; Maccagni & Tarenghi 1981; Schwartz et al. 1979; Mushotzky et al. 1978), and several complete samples of BL Lac objects have been derived from X-ray surveys (Perlman et al. 1996a; Schachter et al. 1993; Stocke et al. 1991; Schwartz et al. 1989). The properties of radio-selected BL Lac objects (RBLs) are systematically different from those of X-ray–selected BL Lacs (XBLs), with the latter having flatter spectral energy distributions from radio to X-rays (Ghisellini et al. 1986; Ledden & O'Dell 1985; Stocke et al. 1985), being less polarized (Jannuzi, Smith, & Elston 1994), and having a higher starlight fraction (Morris et al. 1991). This can be explained by orientation provided the radio emission is more highly beamed (into a narrower cone) than the X-ray emission (Maraschi et al. 1986; Ghisellini & Maraschi 1989; Urry, Padovani, & Stickel 1991; Celotti et al. 1993), which is consistent with the apparent 10:1 ratio of XBL to RBL number densities at a fixed X-ray flux (comparing the XBLs from the *Einstein* Extended Medium Sensitivity Survey[3] to the 1 Jy RBLs; Urry et al. 1991; Wolter et al. 1991). Alternatively, the apparent mismatch in number densities and most of the observed differences between XBL and RBL properties can be explained by selection effects operating on their different radio–through–X-ray spectral shapes (Padovani & Giommi 1995; Giommi & Padovani 1994).

The radio–through–X-ray spectral energy distributions of RBLs and XBLs are indeed systematically different, with the observed peak of the emitted power typically at millimeter/IR wavelengths for RBLs and at UV/soft X-ray wavelengths for XBLs (Giommi, Ansari, & Micol 1995), although some "XBL-like" objects are found in radio surveys and vice versa. A clean separation can be made on the basis of the spectral energy distributions by defining objects as low-frequency–peaked BL Lacs (LBLs) or high-frequency–peaked BL Lacs (HBLs) if their ratio of X-ray flux in 0.3–3.5 keV to radio flux density at 5 GHz is smaller than or larger than $10^{-11.5}$, respectively (Padovani & Giommi 1996). Since LBLs are stronger radio sources and HBLs stronger X-ray sources, the selection wavelength has a clear effect on the apparent number densities of the two kinds of BL Lacs, so that, contrary to the apparent dominance of XBLs over RBLs, LBLs could be more numerous than HBLs (Padovani & Giommi 1995; Giommi & Padovani 1994). Whichever species is predominant, the differences between them undoubtedly reflect fundamental physical properties important to the overall understanding of the phenomenon (Urry & Padovani 1995).

Similarly, the relationship of BL Lacs and FSRQs is unclear but of great interest. (Note that at present, only radio-selected samples of FSRQs are available.) The blazar-like nonthermal continuum and properties such as rapid variability and polarization are common to both quasars and BL Lacs, which nominally differ only in their emission-line properties. An evolutionary link between BL Lacs and FSRQs may explain the correlation of broadband properties with redshift (Vagnetti, Giallongo, & Cavaliere 1991), although this suggestion was based on few (four) BL Lacs which were later found to have broad emission lines; it does not appear to be supported by the broadband and emission-line properties of larger samples (Padovani 1992a). Continuity of the radio and X-ray luminosity functions also suggests a continuity of some kind between RBLs and FSRQs (Maraschi & Rovetti 1994).

Understanding the connections among XBLs, RBLs, and FSRQs will substantially advance our understanding of the fundamental nature of blazars. In this paper, we address these connections via the spectral energy distributions of complete samples of the three blazar subclasses: the 1 Jy RBL sample (Stickel et al. 1991); the EMSS XBL sample (Morris et al. 1991), with the addition of a new XBL from the same survey, previously misclassified as a cluster of galaxies (Perlman et al. 1996b); and a small but complete sample of FSRQs (Brunner et al. 1994) drawn from the S5 radio survey, which includes all flat radio spectrum sources brighter than 1 Jy at 5 GHz (Kühr et al. 1981), with declination $>70°$ and Galactic latitude $>10°$. This sample will be referred to in the following as S5 FSRQ sample.

The 1 Jy RBLs, the EMSS XBLs, and the S5 FSRQs are the largest complete samples of the three kinds of blazars observed in pointed mode with the *ROSAT* Position Sensitive Proportional Counter (PSPC). The dominant emission mechanisms in both BL Lacs and FSRQs are most likely synchrotron emission from radio to UV/soft X-ray frequencies and inverse-Compton scattering for hard X-ray and γ-ray energies, so X-ray spectra are important for determining the relative importance of the two components and for establishing the presence of an inverse-Compton component that extends to γ-ray energies.

We combined the *ROSAT* data with nonsimultaneous fluxes at other wavelengths from the literature. The data selection and analysis are described in § 2. In § 3 the broadband spectra of the different samples are compared, using two-point spectral indices and a composite optical–to–X-ray index that measures the concavity/convexity of the energy distribution between these two bands. In § 4 we describe fits to the broadband spectra with a parabolic function that allowed us to derive reasonable estimates of the apparent bolometric luminosities and the frequencies at which the power per decade peaks. In § 5 we explore the correlations among the spectral shape parameters, luminosity, and redshift. In § 6 we discuss the different types of spectral energy distributions in terms of synchrotron self-Compton models in general, and inhomogeneous jet models in particular, considering both a systematic change of viewing angle in an accelerated jet model and a systematic change in intrinsic physical parameters in a constant velocity jet. Results and conclusions are summarized in § 7.

2. MULTIFREQUENCY DATA FOR THE BLAZAR SAMPLES

In general, no simultaneous observations are available for most of the objects of our samples, so in order to have information about the continuum emission on the whole electromagnetic range we relied on nonsimultaneous data available in the literature. Radio, IR, optical, and UV fluxes

[3] The *Einstein* Extended Medium Sensitivity Survey (EMSS) is a deep ($f_X \gtrsim 5 \times 10^{-14}$ ergs cm^{-2} s^{-1}) X-ray survey in the energy range 0.3–3.5 keV (see Stocke et al. 1991 and references therein).

[4] NED is operated by the Jet Propulsion Laboratory, California Institute of Technology, under contract with the National Aeronautics and Space Administration.

for each source were collected using the NASA/IPAC Extragalactic Database (NED).[4] We restricted our search to publications from the last 15 years, in order to maximize homogeneity and uniformity in the data acquisition, except in the case of the radio data for RBLs and FSRQs, for which most of the measurements were done at earlier epochs.

For each object we averaged the flux densities at each given frequency and assigned as uncertainty the error on the mean (i.e., the rms dispersion σ divided by the square root of N, where N is the number of observations). In cases in which fewer than three measurements were available, we assigned instead an error bar to the flux corresponding to an rms variation of a factor of 1.5. To show the basis for this, we plot in Figure 1 the rms dispersions normalized to the corresponding average fluxes versus the number of observations for objects in the RBL sample with two or more measurements. Since the data for XBLs and FSRQs are insufficient to discuss variability as a function of frequency, in the absence of other information we shall assume XBLs and FSRQs behave the same as RBLs. Different symbols correspond to frequencies in the radio (5 GHz), millimeter (230 GHz), IR (1.36×10^{14} Hz, or K band), and optical (5.45×10^{14} Hz, or V band). Where many fluxes are available, the mean is well defined; for few flux values, we want to assign the largest reasonable uncertainty so as to avoid weighting the point too heavily in the parabolic fits (see § 3.2). An rms value of 1.5 (*solid line*) represents the largest plausible value of the average variation in this sample. We assigned the same error bar to the *ROSAT* PSPC fluxes, as such variability is not uncommon in the X-ray fluxes of XBLs and RBLs (Della Ceca et al. 1990; Sambruna et al. 1994a, b). For the RBL sample as a whole, there is no systematic trend for the variability amplitude to depend on frequency, although for a few well-observed objects (e.g., 0235+164, 0851+202, 1308+326), the rms increases with increasing frequency, in agreement with earlier results (Impey & Neuegebauer 1988; Celotti, Marschi, & Treves 1991, and references therein).

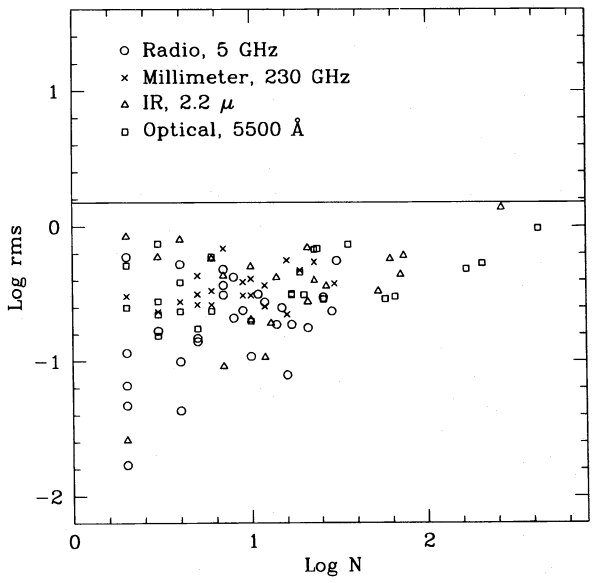

FIG. 1.—Root mean square dispersions (normalized to the corresponding average fluxes) vs. the number of observations for different observing wavelengths. Only data from the RBL sample, which includes well-observed objects, have been used. No trend with the wavelength is apparent for the whole sample. The horizontal solid line represents the upper envelope to the distribution of average variations, a factor 1.5, reached asymptotically as the number of monitoring observations increases. In cases in which few flux measurements are available, the conservative assumption is to allow for an uncertainty of that magnitude.

Table 1 presents the data used in our study: a compilation of average fluxes at radio (5 GHz), millimeter (230 GHz), IR (2.2 μm, or K band), optical (5500 Å, or V band), and X-ray (1 keV) frequencies for each source. When not done in the original reference, the data were corrected for Galactic extinction, following the law of Cardelli, Clayton, & Mathis (1989), and assuming $R = 3.09 \pm 0.06$ (Rieke & Lebofsky 1985) and $N_H/E(B-V) = 5.2 \times 10^{21}$ cm^{-2} mag^{-1} (Shull & Van Steenberg 1985). The line-of-sight column density, N_H, was derived from the 21 cm measurements of Elvis, Lockman, & Wilkes (1989), when available, or Stark et al. (1992) otherwise. Also listed in Table 1 are the observed rms dispersions and the number of observations (in parentheses). The references from which the individual fluxes were taken are listed in Table A1 in the Appendix. The rms dispersions in Table 1 are actually the observed values; as discussed above, in the cases of two data points or less, a fixed (1.5) value will be assigned in the construction of the spectral distributions studied below. While the RBL sample includes several well-observed objects, XBLs and FSRQs are relatively scarcely sampled. In the case of the FSRQs, IR data (which in the rest frame of these high-z objects correspond to emission in the optical range) are totally lacking, and only one recorded value of the V or B magnitude was available from Véron-Cetty & Véron (1993). The B magnitudes have been converted to visual using $B-V = 0.4$ (Padovani 1992b).

Several blazars in our sample have been detected in γ-rays with EGRET (von Montigny et al. 1995; Thompson et al. 1995). These include six RBLs (0235+164, 0537−441, 0716+714, 0735+178, 0954+658 plus the recent addition of 2200+420; R. Hartmann 1995, private communication), and one FSRQ, 0836+710. The γ-ray data are included in the analysis when discussing the theoretical interpretation of individual spectral energy distributions (§§ 5–6). For specific studies of the continuum properties of the γ-ray–loud blazars, including the objects mentioned above, we refer to von Montigny et al. (1995) and Dondi & Ghisellini (1995).

We constructed rest-frame spectral energy distributions using the fluxes of Table 1 multiplied by the observed frequency ν and plotted against $\nu \times (1 + z)$. Composite spectral indices connecting rest-frame fluxes in radio, optical, and X-ray bands were calculated after K-correcting the flux densities reported in Table 1. For the K-correction, the flux densities were multiplied by $(1+z)^{\alpha-1}$, where α is the power-law spectral index in the appropriate energy band ($F_\nu \propto \nu^{-\alpha}$). For RBLs and FSRQs, we used individual spectral indices in the radio provided by Kühr et al. (1981), while for XBLs we assumed $\alpha_r = 0$. In the millimeter, IR, and optical, we used average spectral indices for each class of objects, derived from the literature for the same or similar samples. Specifically, for RBLs we used $\langle\alpha_{mm}\rangle = 0.26$, $\langle\alpha_{IR}\rangle = 1.27$, and $\langle\alpha_{opt}\rangle = 1.05$ (Falomo, Scarpa, & Bersanelli 1994), for XBLs, $\langle\alpha_{IR}\rangle = 0.59$ and $\langle\alpha_{opt}\rangle = 0.65$ (Falomo et al. 1994), and for FSRQs, $\langle\alpha_{mm}\rangle = 0.18$ (Impey & Neugebauer 1988) and $\langle\alpha_{opt}\rangle = 1.38$, derived from UV observations of blazars (Pian & Treves 1993) because the observed V fluxes correspond to emission in the UV region in the rest frame of

TABLE 1

MULTIFREQUENCY DATA FOR BLAZARS

Object	Radio (5 GHz)[a] (Jy)	Millimeter (230 GHz)[a] (Jy)	IR (2.2 μm)[a] (mJy)	Optical (5500 Å)[a] (mJy)	X-Rays (1 keV)[b] (μJy)
EMSS XBLs					
0122.1+0903.....	0.0014	...	0.5	0.047 ± 0.001 (2)	0.05
0158.5+0019.....	0.0113	...	...	0.21 ± 0.06 (3)	1.2
0205.7+3509.....	0.0036	...	0.5	0.10 ± 0.005 (3)	0.90
0257.9+3429.....	0.010	...	1.34	0.25 ± 0.02 (8)	0.10
0317.0+1834.....	0.017	...	0.036	0.36 ± 0.09 (30)	0.54
0419.3+1943.....	0.008	...	0.51	0.09	0.75
0607.9+7108.....	0.0182	...	...	0.09	0.07
0737.9+7441.....	0.024	...	...	0.64	1.30
0922.9+7459.....	0.0033	...	...	0.044 ± 0.002	0.21
0950.9+4929.....	0.0033	...	0.02	0.122 ± 0.04 (5)	0.27
1019.0+5139.....	0.0024	...	...	0.22	0.93
1207.9+3945.....	0.0058	...	0.38 ± 0.14 (2)	0.10	0.55
1221.8+2452.....	0.0264	0.0049	0.95 ± 0.04 (2)	0.42 ± 0.09 (18)	0.18
1229.2+6430.....	0.042	0.0052	...	0.55 ± 0.17 (3)	2.05
1235.4+6315.....	0.007	...	...	0.14 ± 0.02 (4)	0.31
1402.3+0416.....	0.0208	0.0224	2.52 ± 0.30 (6)	0.88 ± 0.37 (17)	0.68
1407.9+5954.....	0.0165	0.0015	0.40 ± 0.23 (2)	0.07 ± 0.01 (3)	0.10
1443.5+6349.....	0.0116	0.001	...	0.06	0.35
1458.8+2249.....	0.0298	...	3.56 ± 0.68 (2)	1.01 ± 0.20 (10)	0.78
1534.8+0148.....	0.034	0.0123	0.92	0.15 ± 0.05 (4)	0.74
1552.1+2020.....	0.0375	...	2.75	0.44 ± 0.08 (10)	2.57
1757.7+7034.....	0.0072	...	...	0.18	0.92
2143.3+0704.....	0.050	0.0222	1.78	0.32 ± 0.04 (15)	0.78
1 Jy RBLs					
0048−097.....	1.110 ± 0.583 (4)	0.670 ± 0.460 (7)	7.23 ± 2.88 (23)	2.41 ± 1.63 (23)	0.77
0118−272.....	1.145 ± 0.075 (2)	0.60	7.86 ± 1.50 (13)	1.92 ± 0.38 (10)	0.20
0235+164.....	1.81 ± 0.54 (26)	1.84 ± 0.87 (19)	15.48 ± 9.36 (74)	1.44 ± 1.06 (36)	1.56
0426−380.....	1.15 ± 0.03 (2)	...	...	0.11	0.09
0454+844.....	1.41 ± 0.14 (4)	0.18 ± 0.06 (6)	...	0.70 ± 0.36 (2)	0.02[c]
0537−441.....	3.93 ± 0.17 (4)	...	9.31 ± 4.70 (10)	1.49 ± 0.43 (26)	0.78
0716+714.....	0.86 ± 0.18 (8)	1.12 ± 0.61 (23)	11.07 ± 8.88 (4)	2.96	1.17
0735+178.....	2.13 ± 0.50 (29)	1.07 ± 0.33 (9)	18.48 ± 8.12 (71)	3.22 ± 1.56 (168)	0.22
0814+425.....	1.86 ± 0.68 (7)	0.57 ± 0.15 (5)	1.99 ± 1.68 (2)	0.26 ± 0.04 (3)	0.05
0851+202.....	2.99 ± 0.56 (17)	3.05 ± 1.15 (30)	18.92 ± 25.93 (267)	6.08 ± 5.91 (434)	0.70 ± 0.25 (2)
0954+658.....	0.90 ± 0.38 (8)	0.47 ± 0.13 (4)	...	0.86 ± 0.24 (3)	0.16
1144−379.....	1.61 ± 0.96 (2)	...	2.78 ± 1.65 (3)	0.62 ± 0.37 (6)	0.41
1147+245.....	0.82 ± 0.12 (5)	0.37 ± 0.16 (5)	8.07 ± 2.23 (21)	1.53 ± 0.36 (6)	0.05
1308+326.....	2.26 ± 0.40 (21)	0.80 ± 0.45 (16)	7.24 ± 5.04 (21)	2.23 ± 1.53 (24)	0.13
1418+546.....	1.22 ± 0.38 (7)	1.15 ± 0.47 (10)	13.20 ± 4.77 (27)	2.72 ± 0.82 (66)	0.30
1519−273.....	2.17 ± 0.25 (2)	0.49	1.27	0.47 ± 0.35 (3)	0.39
1538+149.....	1.53 ± 0.42 (12)	0.43 ± 0.10 (3)	2.36 ± 0.48 (10)	0.32 ± 0.10 (20)	0.09
1652+398.....	1.27 ± 0.10 (16)	0.46 ± 0.14 (2)	40.04 ± 13.20 (53)	15.65 ± 4.52 (58)	8.30
1749+096.....	1.44 ± 0.36 (15)	1.34 ± 0.49 (12)	5.70 ± 2.38 (14)	1.18 ± 0.54 (19)	0.14 ± 0.01 (2)
1749+701.....	1.11 ± 0.35 (11)	0.31 ± 0.12 (9)	...	0.99 ± 0.22 (3)	0.15
1803+784.....	2.79 ± 0.30 (10)	1.03 ± 0.23 (16)	6.7	0.99 ± 0.22 (3)	0.26 ± 0.03 (2)
1807+698.....	1.71 ± 0.32 (14)	0.86 ± 0.27 (5)	21.42 ± 1.95 (7)	7.85 ± 2.44 (17)	0.32
1823+568.....	1.45 ± 0.21 (5)	0.84 ± 0.22 (6)	3.86 ± 0.10 (2)	0.17	0.42
2005−489.....	1.21 ± 0.02 (2)	...	29.25 ± 3.11 (12)	9.85 ± 1.71 (5)	4.12 ± 1.77 (2)
2007+777.....	1.72 ± 0.41 (9)	0.78 ± 0.20 (12)	...	1.17 ± 0.18 (3)	0.17
2131−021.....	1.84 ± 0.31 (3)	...	0.74	0.16 ± 0.04 (2)	0.05
2200+420.....	3.51 ± 1.96 (31)	2.14 ± 0.66 (10)	37.08 ± 21.30 (62)	8.65 ± 4.62 (207)	0.88
2240−260.....	1.03	...	1.96 ± 1.13 (6)	0.26 ± 0.10 (4)	0.07
2254+074.....	0.56 ± 0.27 (7)	...	4.50 ± 1.94 (7)	0.60 ± 0.19 (17)	0.09
S5 FSRQs					
0016+731.....	1.57 ± 0.11 (2)	0.70 ± 0.24 (13)	...	0.32	0.04
0153+744.....	1.56 ± 0.09 (3)	0.06 ± 0.06 (6)	...	0.9	0.06
0212+735.....	2.22 ± 0.13 (3)	0.64 ± 0.30 (15)	...	0.37	0.20
0615+820.....	1.00	0.18 ± 0.08 (5)	...	0.73	0.041 ± 0.006 (2)
0836+710.....	2.60 ± 0.19 (3)	0.42 ± 0.10 (8)	...	1.47	1.73 ± 0.57 (2)
1039+811.....	0.89 ± 0.36 (2)	0.58 ± 0.18 (11)	...	0.24	0.18
1150+812.....	1.14 ± 0.10 (3)	0.61 ± 0.09 (6)	...	0.28	0.09 ± 0.01 (2)
1928+738.....	3.25 ± 0.31 (3)	0.74 ± 0.30 (11)	...	1.44	1.05

[a] References are listed in Appendix A.

[b] X-ray (*ROSAT*) data for XBLs, RBLs, and FSRQs are from Perlman et al. 1996b, Urry et al. 1996, and Brunner et al. 1994, respectively.

[c] From Brunner et al. 1994.

these objects. In the X-rays, we used individual *ROSAT* spectral indices for all objects (Urry et al. 1996; Perlman et al. 1996b; Brunner et al. 1994), as follows. For the RBL sample, we adopted the spectral indices from the most acceptable of two power-law fits, with either Galactic or free absorption (see Table 2 in Urry et al. 1996). For XBLs, we used the spectral indices from Table 1 of Perlman et al. (1996b). For FSRQs, we used spectral slopes derived from the fits with fixed Galactic absorption. For these objects, free-absorption fits could be performed only in four of eight cases because of the limited statistics, and in two of these objects (1150+812 and 1928+738) marginal evidence for excess absorption and steeper slopes was found (Brunner et al. 1994). Because the derived free-fit slopes are affected by very large uncertainties, we used the indices from the fixed-absorption fits for these objects, too. However, our results are not significantly affected by using the free-fit slopes for 1150+812 and 1928+738.

3. SPECTRAL ENERGY DISTRIBUTIONS OF BLAZARS

In order to characterize the shapes of blazar spectral energy distributions, we followed two approaches. The first is to compute broadband spectral indices, and the second is to fit each overall spectra with a parabola.

3.1. *Broadband Spectral Indices*

Two-point (composite) spectral indices were calculated following the usual definition (Ledden & O'Dell 1985):

$$\alpha_{12} = -\frac{\log (F_1/F_2)}{\log (\nu_1/\nu_2)}, \quad (1)$$

where F_1 and F_2 are the flux densities at frequencies ν_1 and ν_2, respectively. For all the objects in our samples we computed the radio–to–optical (α_{ro}), radio–to–X-ray (α_{rx}), and optical–to–X-ray (α_{ox}) indices, using the K-corrected average flux densities at 5 GHz, 5500 Å (V-band), and at 1 keV. The two-point indices for each object are given in Table 2, while average values and rms dispersions for each sample are reported in Table 3A.

The distributions of α_{rx}, α_{ro}, and α_{ox} for the three classes are shown in Figures 2*a*–2*c*, respectively. XBLs (*dashed lines*) have significantly flatter indices than RBLs and FSRQs (*solid lines* and *dotted lines*, respectively), with a Kolmogorov-Smirnov (KS) probability that the corresponding distributions are the same of $P_{KS} < 0.06\%$ for all three indices. In contrast, the distributions of α_{rx}, α_{ro}, and α_{ox} for RBLs and FSRQs are not demonstrably different ($P_{KS} \sim 56\%$, 44%, and 28%, respectively).

In order to describe the energy distributions better between the optical and X-ray spectral regions taking into account the measured spectral shape within the *ROSAT* band, we introduce the index, $\alpha_{xox} = \alpha_{ox} - \alpha_x$, i.e., the difference between α_{ox} and the *ROSAT* PSPC energy index, α_x. A value of α_{xox} near zero indicates that the X-ray spectrum lies on the extrapolation of the optical–to–X-ray slope, while negative or positive values indicate convex or concave optical–to–X-ray continua, respectively. A concavity indicates the presence of a hard spectral component emerging in the X-ray band, which may connect to the γ-ray emission (e.g., 3C 279; Maraschi et al. 1994).

The individual and average values of α_{xox} are given in Tables 2 and 3A, respectively, while the distributions for the samples are shown in Figure 2*d*. On average, α_{xox} is negative for XBLs, which indicates convex (downward curved) continua, while it is positive for FSRQs, corresponding to concave (upward curved) optical–to–X-ray continua. RBLs appear intermediate, with a significant spread in this index extending from very negative to very positive values. The distributions of this spectral index differ at a confidence level of ~99.99% for RBLs versus XBLs and XBLs versus FSRQs and of ~93% for RBLs versus FSRQs. The spread in α_{xox} for the RBL class is directly related to the dispersion in the *ROSAT* spectral indices reported by Urry et al. (1996). Their α_x distribution showed a significant deviation from a Gaussian, with both a steep and a flat tail; those RBLs with very steep or very flat PSPC spectra have very negative or very positive α_{xox}, respectively.

In Figure 3*a* we plot α_{ro} versus α_{xox} for the three blazar samples. As expected from Figures 2*b* and 2*d*, XBLs and RBLs occupy different regions of the diagram. They form a continuous sequence, however, in the sense that objects with smaller α_{ro} have more negative α_{xox} values, i.e., more convex optical–to–X-ray continua, while FSRQs form a "horizontal branch," with a significant overlap with the RBL sample. The XBL with the smallest α_{ro} and the flat optical–to–X-ray continuum is 1019.0+5139, the EMSS source previously classified as a cluster of galaxies (Perlman et al. 1996b). According to a nonparametric Spearman test, α_{ro} is correlated with α_{xox} with probability $P_S = 99.99\%$ (correlation coefficient $\tau_S = 0.527$ and 60 points) for the three samples combined. The correlation is clearly due to the BL Lacs alone, with RBLs and XBLs showing the correlation at a similar confidence level. The correlations for RBLs and XBLs separately are not significant. Using the *ROSAT* slopes α_x, instead of the composite index α_{xox}, we still obtain a spectral sequence analogous to Figure 3*a*, but the anticorrelation of α_{ro} with α_x for the three samples combined is weaker ($P_S \sim 99.8\%$, $\tau_S = -0.352$).

This color-shape analysis shows that different blazar classes have systematically different continuum shapes, in agreement with previous reports (Giommi et al. 1995; Ghisellini et al. 1986; Maraschi et al. 1986; Ledden & O'Dell 1985; Stocke et al. 1985). XBLs differ strongly from RBLs and FSRQs, having flatter overall radio-to-optical spectra and convex optical–to–X-ray continua. RBLs and FSRQs have similar radio-to-optical energy distributions but differ significantly in the shape of the optical–to–X-ray continuum. This was previously noted by Brunner et al. (1994) on the basis of the S5 FSRQs and many fewer (five objects) 1 Jy RBLs. FSRQs have mostly concave continua, while the RBL sample includes concave as well as convex cases. Despite this differences, the three kinds of blazars exhibit a remarkable continuity in their spectral properties, as the color-shape diagram in Figure 3*a* seems to follow a single spectral sequence.

3.2. *Parabolic Fits*

Another way of characterizing the continuum shape of blazars, instead of using two-point indices, is to fit a continuous curve to the spectral energy distribution of each object. This has the advantage of taking into account more data and represents a consistent, reasonably robust way to determine such interesting parameters as the bolometric luminosity and the frequency at which the bulk of the radiation is emitted.

Following Landau et al. (1986) we chose to parameterize the power per decade energy distribution in terms of a

TABLE 2

MULTIFREQUENCY PROPERTIES OF BLAZARS

Object	z	α_{rx}	α_{ro}	α_{ox}	$\alpha_{ox} - \alpha_x$	log L_B (ergs s^{-1})	log ν_p (Hz)	log ($\nu_p L_p$) (ergs s^{-1})
XBLs								
0122.1+0903.....	0.339	0.58	0.30	1.13	0.52	45.19	13.47	44.51
0158.5+0019.....	0.299	0.51	0.33	0.86	−0.60	45.84	16.87	44.89
0205.7+3509.....	0.318	0.46	0.32	0.72	−0.98	45.47	17.51	44.55
0257.9+3429.....	0.247	0.65	0.33	1.25	−0.42	45.12	14.88	44.24
0317.0+1834.....	0.190	0.58	0.33	1.05	−0.27	45.11	14.36	44.27
0419.3+1943.....	0.512	0.53	0.40	0.78	0.06	45.76	13.83	45.00
0607.9+7108.....	0.267	0.70	0.47	1.15	−0.06	44.98	15.25	44.04
0737.9+7441.....	0.315	0.56	0.32	1.00	0.09	46.19	16.16	45.21
0922.9+7459.....	0.638	0.55	0.38	0.87	0.09	45.85	17.21	44.91
0950.9+4929.....	0.207	0.51	0.30	0.91	−0.85	46.07	16.66	45.13
1019.0+5139.....	0.141	0.45	0.21	0.90	0.38	45.21	16.85	44.30
1207.9+3945.....	0.615	0.52	0.35	0.84	−0.29	46.18	16.75	45.24
1221.8+2452.....	0.218	0.67	0.36	1.24	−0.23	45.27	15.27	44.36
1229.2+6430.....	0.164	0.56	0.38	0.91	−0.08	45.54	17.23	44.60
1235.4+6315.....	0.297	0.55	0.34	0.95	−0.96	45.24	14.88	44.35
1402.3+0416.....	0.200	0.57	0.28	1.14	−0.71	45.51	14.85	44.64
1407.9+5954.....	0.495	0.66	0.48	1.00	−0.74	45.47	15.90	44.50
1443.5+6349.....	0.299	0.58	0.47	0.81	−0.29	45.16	19.57	44.41
1458.8+2249.....	0.235	0.58	0.29	1.14	−1.17	45.90	15.40	45.00
1534.8+0148.....	0.312	0.61	0.47	0.88	−0.01	45.67	16.88	44.70
1552.1+2020.....	0.222	0.54	0.39	0.84	0.05	45.51	13.70	44.74
1757.7+7034.....	0.407	0.50	0.33	0.84	−0.28	46.02	17.18	45.09
2143.3+0704.....	0.237	0.61	0.44	0.94	−0.97	45.65	16.34	44.67
RBLs								
0048−097	...	0.75	0.51	1.28	−0.29	47.07	13.84	46.22
0118−272	>0.557	0.86	0.52	1.49	0.29	46.91	14.49	46.00
0235+164	0.940	0.76	0.61	1.04	−0.75	47.52	13.39	46.72
0426−380	>1.030	0.90	0.75	1.18	0.23	46.77	13.22	45.91
0454+844	0.112	1.01	0.65	1.71	0.28	44.39	13.81[a]	43.38
0537−441	0.896	0.82	0.62	1.24	0.20	47.53	14.07	46.62
0716+714	>0.300	0.75	0.50	1.24	−0.53	46.50	13.79	45.68
0735+178	>0.424	0.88	0.53	1.56	0.36	47.05	14.03	46.19
0814+425	0.258	0.98	0.74	1.44	1.28	45.49	13.34	44.61
0851+202	0.306	0.84	0.51	1.47	0.09	46.85	13.72	46.03
0954+658	0.367	0.88	0.58	1.45	1.21	46.29	14.09	45.39
1144−379	1.048	0.82	0.65	1.14	−0.40	47.38	13.75	46.54
1147+245	...	0.92	0.52	1.70	0.84	47.04	14.58	46.13
1308+326	0.997	0.91	0.55	1.60	0.65	47.63	13.83	46.78
1418+546	0.152	0.85	0.52	1.49	0.37	45.95	13.85	45.11
1519−273	...	0.86	0.70	1.16	0.13	46.66	13.17	45.87
1538+149	0.605	0.93	0.67	1.42	0.76	46.62	13.56	45.74
1652+398	0.033	0.67	0.38	1.24	−0.39	45.05	13.94	44.24
1749+096	0.320	0.92	0.61	1.49	0.86	46.56	13.27	45.78
1749+701	0.770	0.81	0.52	1.37	−0.40	47.05	14.43	46.13
1803+784	0.679	0.88	0.68	1.28	0.28	46.97	13.43	46.12
1807+698	0.051	0.87	0.46	1.66	0.85	44.96	14.26	44.06
1823+568	0.664	0.85	0.75	1.06	0.91	46.87	13.65	46.01
2005−489	0.071	0.71	0.41	1.28	−0.71	46.35	18.26	45.47
2007+777	0.342	0.91	0.62	1.47	0.81	46.34	13.66	45.48
2131−021	0.557?	0.96	0.77	1.33	0.28	46.36	13.16	45.50
2200+420	0.069	0.85	0.51	1.50	0.55	45.56	14.25	44.66
2240−260	0.774	0.89	0.66	1.33	0.18	46.75	13.32	45.93
2254+074	0.190	0.88	0.59	1.43	0.31	45.76	13.25	44.99
FSRQs								
0016+731	1.781	1.02	0.62	1.76	1.76	47.86	13.56	47.03
0153+744	2.338	0.91	0.47	1.76	1.41	47.60	14.75[a]	46.54
0212+735	2.367	0.95	0.59	1.62	2.18	47.99	13.30	47.17
0615+820	0.710	0.92	0.56	1.61	0.36	46.44	14.15[a]	45.50
0836+710	2.170	0.76	0.47	1.31	0.90	48.46	15.95[a]	47.43
1039+811	1.260	0.80	0.58	1.22	0.13	47.21	13.29	46.38
1150+812	1.250	0.90	0.62	1.44	0.96	47.26	13.40	46.44
1928+738	0.302	0.83	0.63	1.21	0.41	46.22	13.68	45.31

[a] Upper limit (see text).

TABLE 3

AVERAGE SPECTRAL PARAMETERS

Class	$\langle\alpha_{rx}\rangle$	$\langle\alpha_{ro}\rangle$	$\langle\alpha_{ox}\rangle$	$\langle\alpha_{ox}-\alpha_x\rangle$	$\langle\log L_B\rangle$ (ergs s^{-1})	$\langle\log \nu_p\rangle$ (Hz)
A. Complete Samples						
EMSS XBLs.....	0.57 ± 0.06	0.36 ± 0.07	0.96 ± 0.15	−0.34 ± 0.46	45.57 ± 0.37	15.93 ± 1.45
1 Jy RBLs	0.86 ± 0.08	0.59 ± 0.10	1.38 ± 0.18	0.26 ± 0.54	46.49 ± 0.80	13.91 ± 0.93
S5 FSRQs	0.89 ± 0.09	0.57 ± 0.06	1.49 ± 0.23	1.01 ± 0.72	47.38 ± 0.76	14.01 ± 0.93
B. RBL Subgroups						
XBL-like	0.74 ± 0.03	0.51 ± 0.10	1.19 ± 0.13	−0.66 ± 0.12	46.79 ± 0.64	15.15 ± 2.70
Intermediate.....	0.86 ± 0.08	0.60 ± 0.10	1.36 ± 0.16	0.09 ± 0.29	46.53 ± 0.85	13.72 ± 0.43
FSRQ-like	0.90 ± 0.04	0.60 ± 0.10	1.48 ± 0.18	0.87 ± 0.22	46.34 ± 0.80	13.85 ± 0.43

logarithmic parabola of the form

$$\log(\nu L_\nu) = A(\log \nu)^2 + B \log \nu + C . \quad (2)$$

Note that Landau et al. used a similar expression to parameterize the spectral flux distribution in log F_ν versus log ν, which requires only a redefinition of the constants.

Equation (2) implicitly assumes that all the data belong to a smooth emission component. While it is likely that the

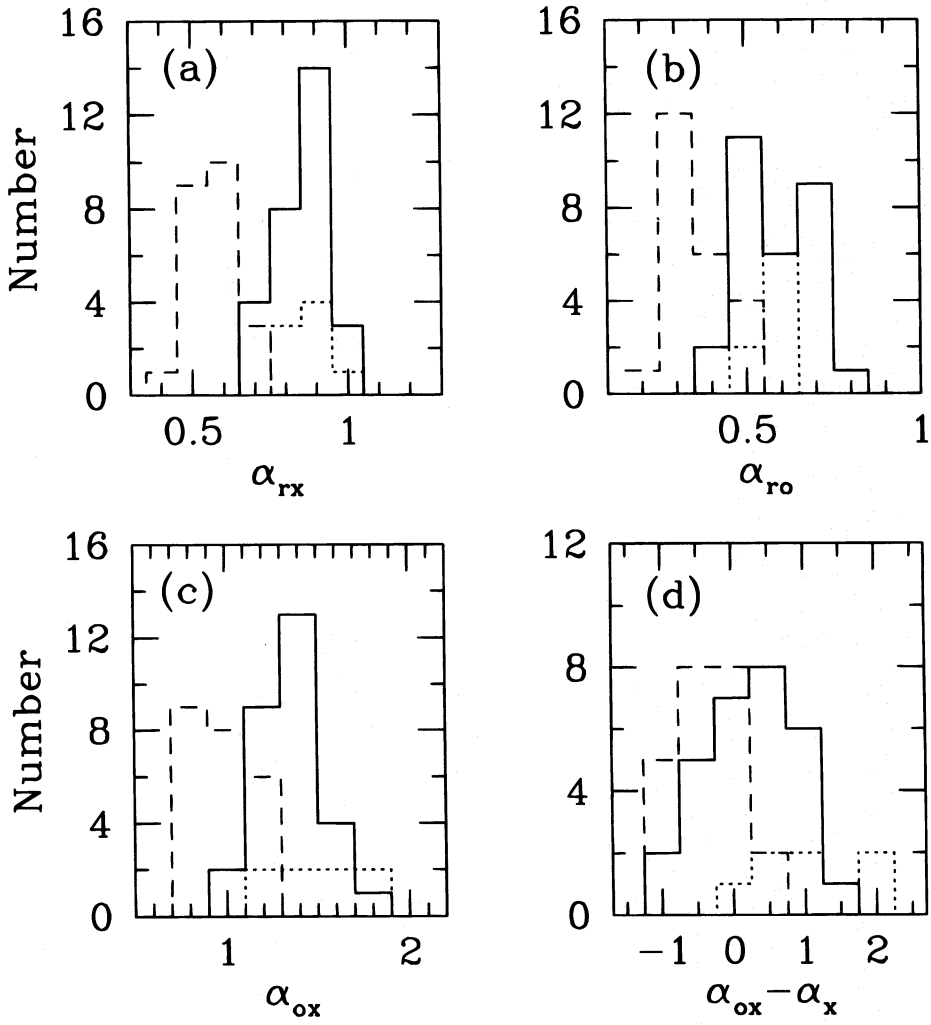

FIG. 2.—Distributions of the composite spectral indices for the EMSS XBLs (*dashed line*), the 1 Jy RBLs (*solid line*), and the S5 FSRQs (*dotted line*). (*a*): radio–to–X-ray index, α_{rx}, (*b*): radio-to-optical index, α_{ro}, (*c*): optical–to–X-ray index, α_{ox}. In all three cases, XBLs are well separated from both RBLs and FSRQs, at a confidence >99.9% from a Kolmogorov-Smirnov test, and they have flatter indices. RBLs and FSRQs do not differ significantly from one another. (*d*): distribution of $\alpha_{xox} = \alpha_{ox} - \alpha_x$, where α_x is the *ROSAT* PSPC energy spectral index. This composite index describes the shape of the optical–to–X-ray continuum: negative (positive) values of α_{xox} indicate downward, or convex (upward, or concave) continuum emission. XBLs have mostly negative indices, indicating typically convex spectra, at variance with FSRQs, which have concave continua. RBLs have a large spread of optical–to–X-ray shapes. The three distributions are all different (at ~99.99% confidence for XBLs vs. either RBLs or FSRQs and at 93.4% confidence for RBLs vs. FSRQs).

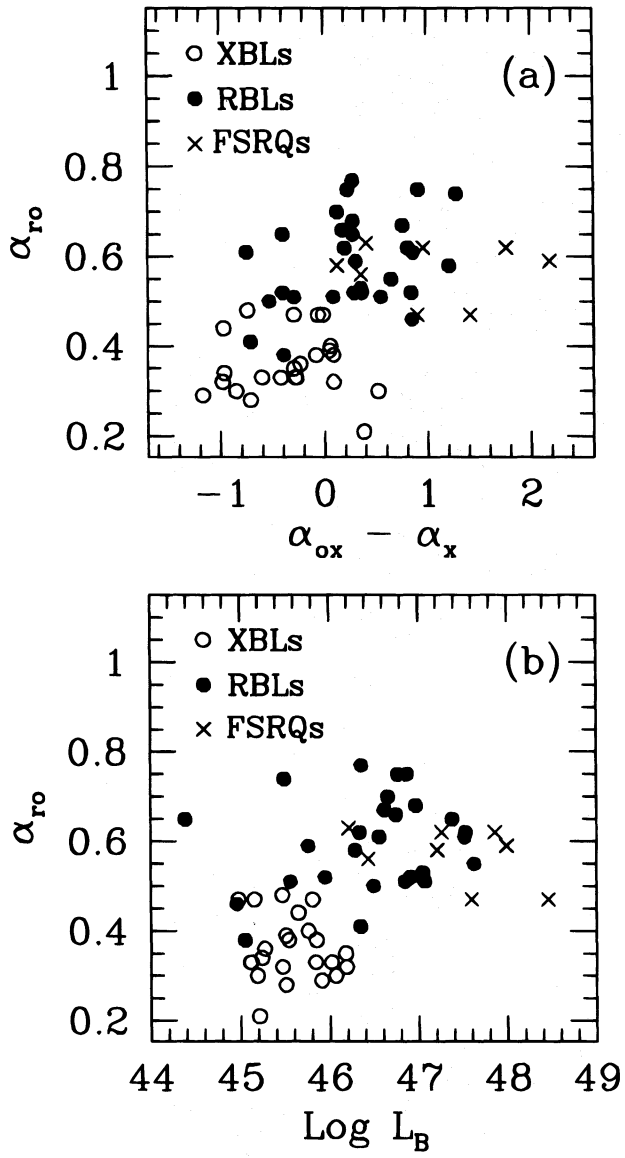

FIG. 3.—(*a*) Color-shape plot of blazar spectra, with the radio-to-optical index, α_{ro}, vs. the concavity/convexity indicator, $\alpha_{xox} = \alpha_{ox} - \alpha_x$. The three blazar classes occupy different but overlapping regions, indicating a continuity of properties. There is a correlation at a significance level of 99.99% (from a Spearman nonparametric test), in the sense that objects with steeper α_{ro} have flatter α_{xox}. (*b*) Plot of the radio-to-optical index, α_{ro}, vs. the bolometric luminosity, as estimated from parabolic fits to the multiwavelength spectra. There is a correlation at >99% confidence, in the sense of more luminous objects having steeper α_{ro} indices or, as α_{ro} is strictly correlated with the peak frequency of the emission, lower ν_p.

radio through UV emission is generated by the same (synchrotron) process (e.g., Bregman, Maraschi, & Urry 1987), this is not necessarily true of the X-ray continuum in all objects. In fact the observed distributions of α_{xox} (Fig. 2*d*) show that while for XBLs the hypothesis that the X-ray continuum is an extension of the optical synchrotron component is reasonable, this is not true for FSRQs and for those RBLs that have a concave optical–to–X-ray continuum. In the latter cases, the X-ray emission probably originates from a different process, most likely inverse-Compton (see §§ 6 and 7). This motivated us to include the X-ray data point in the fits only in those cases with $\alpha_{xox} < 0$, i.e., when the X-ray spectrum connects smoothly to the optical continuum. However, in four cases with particularly poor sampling (the FSRQs 0153+744, 0615+820, and 0836+710, and the RBL 0454+844), the X-ray data points had to be included in the fit in order to constrain the shape of the parabola at the higher energies. The derived values of ν_p thus represent upper limits in these four cases.

For each object of the three samples, we constructed the luminosity per decade distribution in the rest frame of the source using the data in Table 1 plus additional data at other frequencies (mostly taken from the references listed in the Appendix). The flux densities were converted to luminosities using $H_0 = 75$ km s^{-1} Mpc^{-1} and $q_0 = 0.5$, assuming isotropic emission. A few RBLs do not have redshift determinations; an average sample value of $z = 0.56$ was assigned to these cases, while for those sources with an estimated redshift from intervening absorption systems, we used the lower limit. The derived powers per decade and uncertainties (obtained with the criteria described in § 2) were plotted versus the frequency multiplied by $(1 + z)$ to derive rest-frame spectral distributions.

The last three columns of Table 2 list the bolometric luminosities, L_B, the peak frequencies, ν_p, and the luminosity at the peak frequency, L_p, derived from the parabolic fits, and average values of these three quantities for the classes are given in Table 3A. Figures 4*a*–4*c* shows the spectral energy distributions and the parabolic fits for the three samples; solid lines were used to plot the fits when the X-ray point was included, and dashed lines were used, otherwise.

The bolometric luminosity was calculated over the frequency range log $\nu = 9$–19, which represents the energy interval in which the synchrotron emission is radiated. Excluding other frequencies below this range underestimates the synchrotron flux by a negligible fraction (<0.1%). The lost fraction above 10^{19} Hz is typically <1%, more severe ($\gtrsim$60%) only in the two worst cases of 2005−489 and 1443.5+6349. Moreover, the exclusion of the γ-ray range, where in some cases the power output is larger than in all other bands, can underestimate the total power by a much larger fraction. For example, for 0235+134, integrating the EGRET spectrum (Hunter et al. 1993) between 100 MeV and 5 GeV yields a luminosity of 2×10^{48} ergs s^{-1}, 1 order of magnitude higher than in Table 2. The same calculation for 0537−441 (EGRET spectrum from Thompson et al. 1993a), yields 4.5×10^{47} ergs s^{-1}, comparable to L_B in Table 2. Given the scarcity of data, a systematic analysis including the γ-ray observations is not allowed here.

In several sources the reduced χ^2 from the parabolic fits is rather high (>2), which indicates that a parabola is not a good representation of the spectral energy distributions. Obviously we do not attribute a physical meaning to this shape but use it as a simple parameterization of the continuum over 10 decades in frequency, in order to determine the bolometric luminosity and the peak frequency. We note that, of these two parameters, the latter is more sensitive to the quality and quantity of the spectral data; for example, the inclusion or exclusion of the X-ray data point can change the estimate of the peak frequency by more than 3 orders of magnitude in several objects. It is therefore clear that multifrequency simultaneous data are crucial for an accurate determination of ν_p. In contrast, over the fiducial range $\nu = 10^9$–10^{19} Hz, the bolometric luminosity is much less sensitive to the X-ray data points, since it is affected only by a factor $\approx$2 by their inclusion/exclusion.

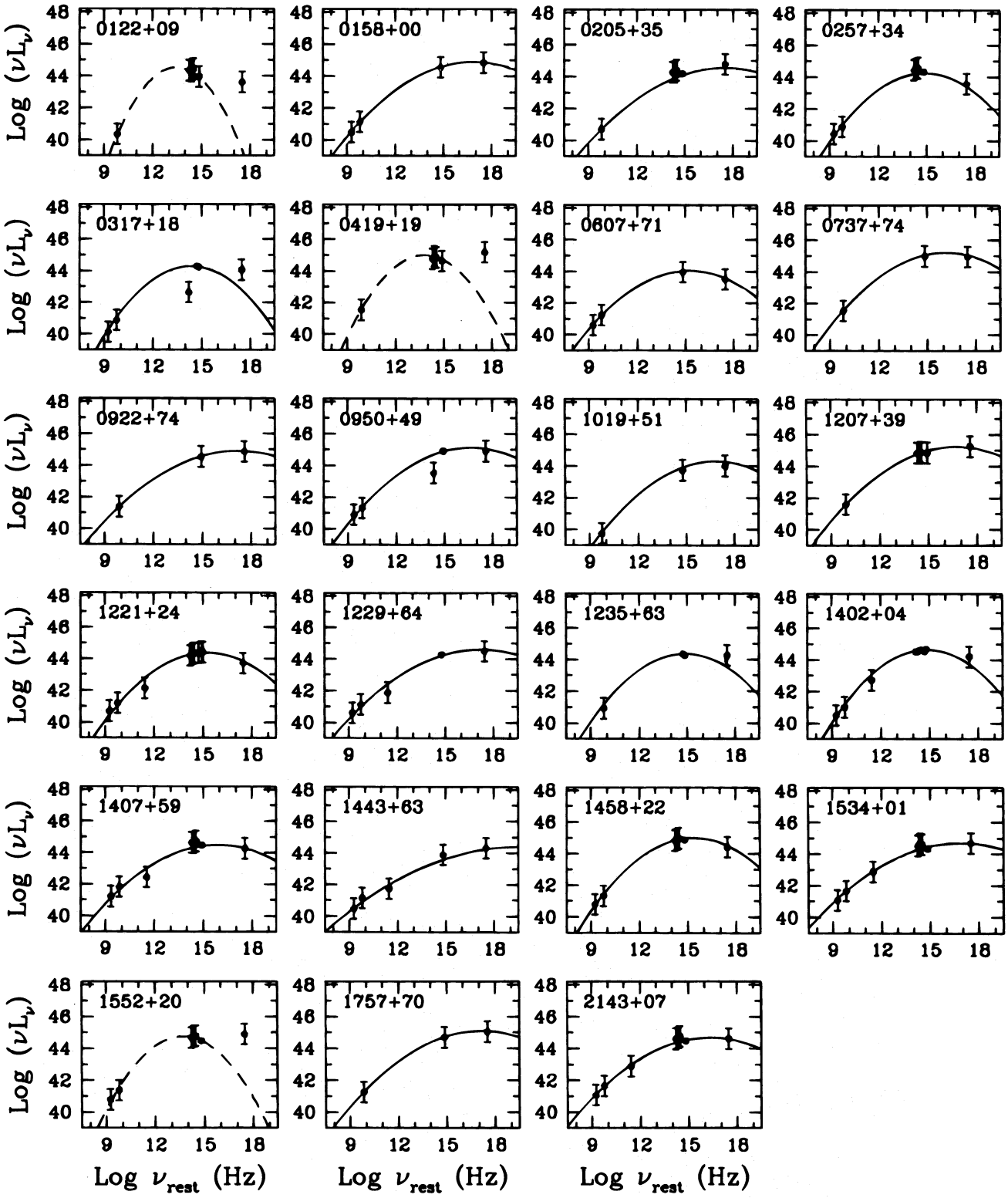

FIG. 4*a*

FIG. 4.—Multifrequency spectral energy distributions of (*a*) the EMSS XBLs, (*b*) the 1 Jy RBLs, and (*c*) the S5 FSRQs. The intrinsic power (νL_ν, in ergs s^{-1}) is plotted vs. the rest-frame frequency, $\nu_{rest} = \nu_{obs} \times (1 + z)$ (in Hz). The radio to UV data were derived from averaging independent, nonsimultaneous published observations, while the X-ray flux densities are from the *ROSAT* PSPC measurements (Table 1). The error bars are the errors of the mean, i.e., rms dispersions divided by the square root of the number of observations N, when $N \geq 3$; for $N = 1$ or 2, they represent a factor of 1.5 in possible variability. The solid line is the parabolic fit to the individual spectral energy distributions including the X-ray data point (cases of convex optical–to–X-ray continua), the dashed line is the parabolic fit excluding this point (cases of concave optical–to–X-ray continua). Note the spread in the peak of the parabola, which can be as low as 10^{13} and as high as 10^{17} Hz.

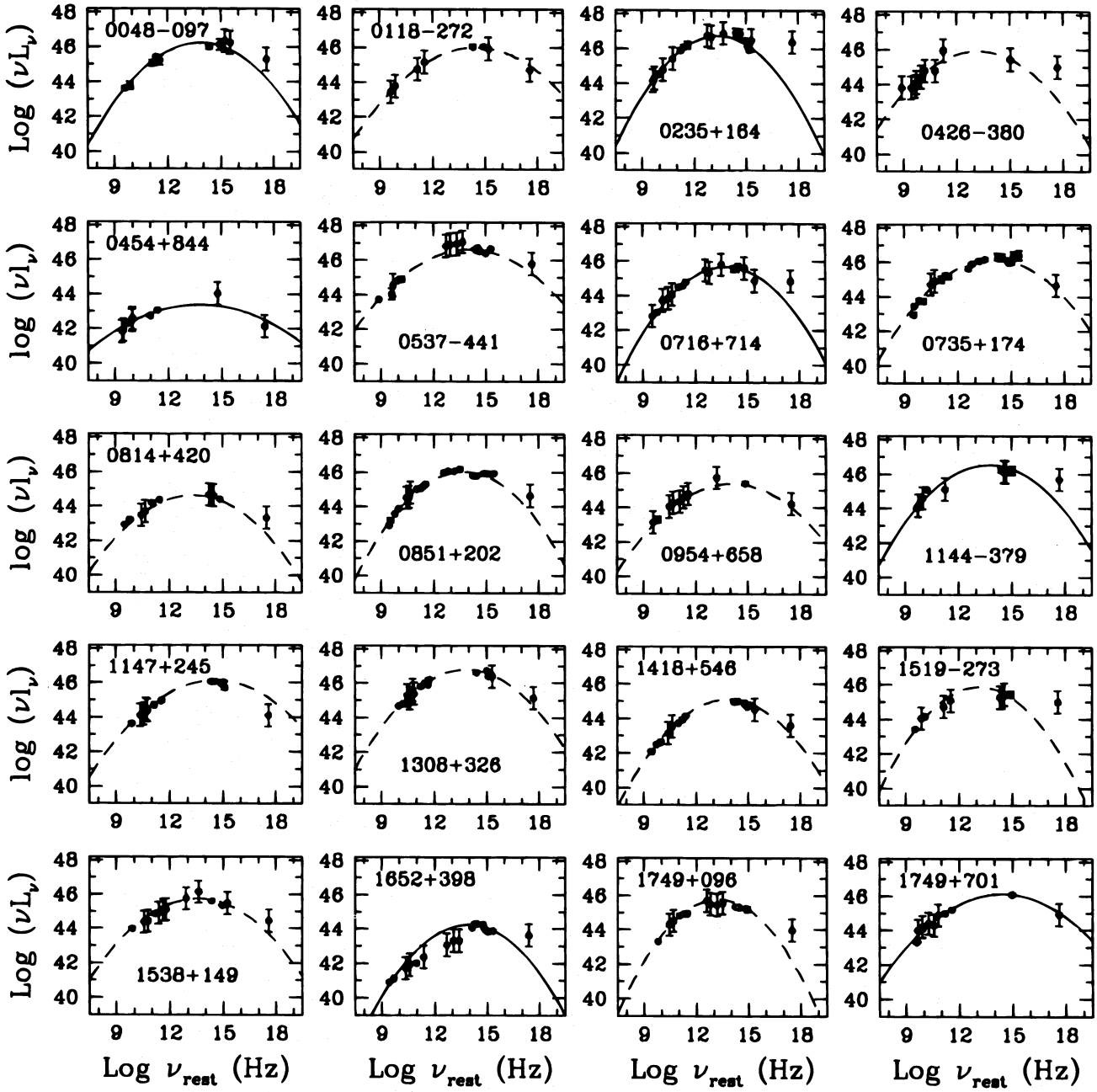

FIG. 4*b*

Table 3A shows that the average bolometric luminosity increases going from XBLs to RBLs to FSRQs. On average, XBLs are less luminous that RBLs and FSRQs at 99.99% confidence, while the latter have higher bolometric luminosities than RBLs at 98.2% confidence. In addition, XBLs have higher (at >99.99%) cutoff frequencies than RBLs and FSRQs, while the ν_p distributions of the latter two samples are not demonstrably different (the probability that they are different is only 7%). The cutoff frequencies are plotted versus the bolometric luminosities in Figure 5. More luminous sources are clustered at lower values of ν_p, although no object has a cutoff frequency lower than 10^{13} Hz. We note that it is unlikely that the cutoff frequency could assume much smaller values, since below $\sim 10^{11}$ Hz the synchrotron self-absorption process becomes important.

From the values of L_B and L_p in Table 2 one can derive a useful bolometric correction for the three samples. It appears to be similar in all cases, with average values $\langle L_B/L_p\rangle_{\rm XBLs} = 8.20 \pm 1.25$, $\langle L_B/L_p\rangle_{\rm RBLs} = 7.29 \pm 0.88$, and $\langle L_B/L_p\rangle_{\rm FSRQs} = 8.22 \pm 1.95$.

4. CORRELATIONS OF SPECTRAL PARAMETERS WITH LUMINOSITY AND REDSHIFT

As discussed above, blazars form a continuous sequence in the $\alpha_{\rm xox} - \alpha_{\rm ro}$ plane (Fig. 3*a*), with XBLs having flatter radio-to-optical indices and more convex optical–to–X-ray continua than RBLs and FSRQs. The XBL to RBL to FSRQ sequence, as shown in Table 3A, corresponds roughly to increasing L_B and z. Here we examine more closely these correlations.

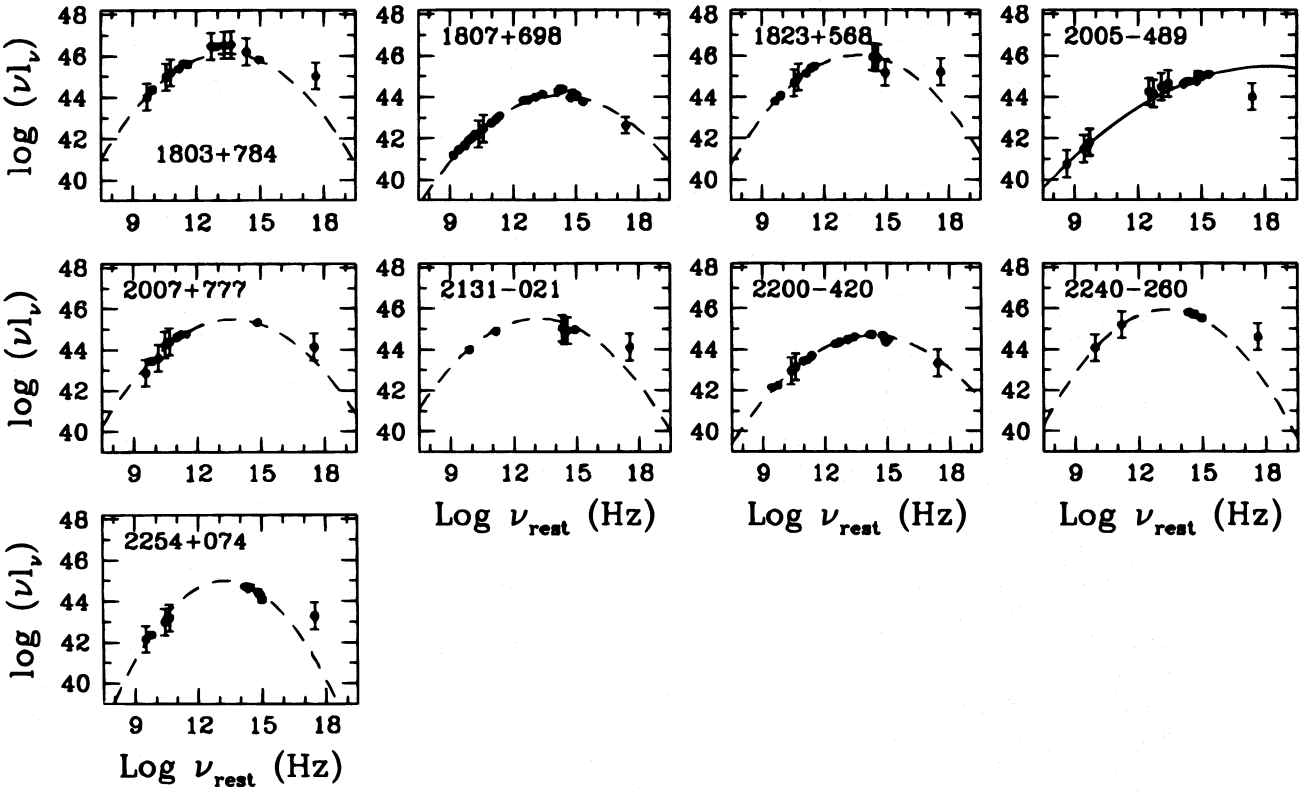

FIG. 4b—*Continued*

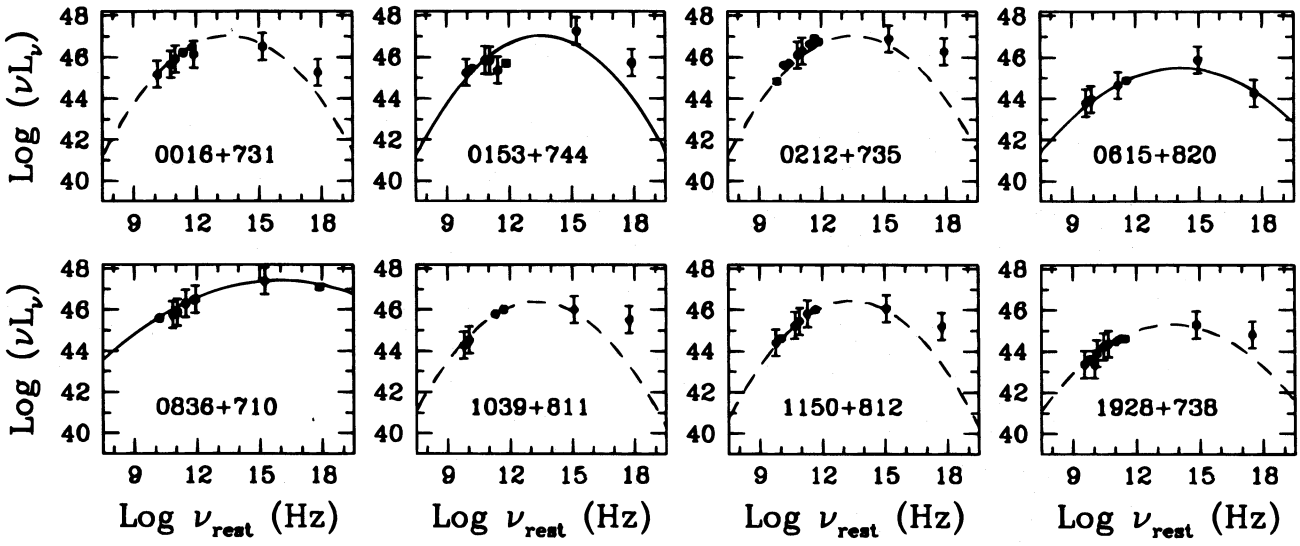

FIG. 4c

Not all the parameters in Table 2 are independent. The index α_{rx} can be written as a combination of α_{ro} and α_{ox}. The peak frequency, ν_p, is closely related to α_{ro}, which is a measure of how fast the continuum rises from radio toward the peak of the synchrotron emission and is therefore steeper for objects with the emission peak at lower energies. Indeed, α_{ro} and ν_p are very well correlated, with $P_S > 99.999\%$ (see also Comastri, Molendi, & Ghisellini 1996). The decrease in α_{ro} from 0.8 to 0.3 corresponds to an increase in ν_p from 10^{13} to 10^{18} Hz. This leaves three independent quantities. We choose to discuss α_{ro} instead of ν_p because the latter is poorly determined in some of the fits. We also choose α_{xox} because it describes the shape of the high-energy emission. Finally, we choose L_B, which differs from the peak luminosity by a nearly constant factor (see above) and has a clear physical meaning; it is very well correlated with redshift in the usual way for flux-limited samples, so we discuss correlations with the latter quantity

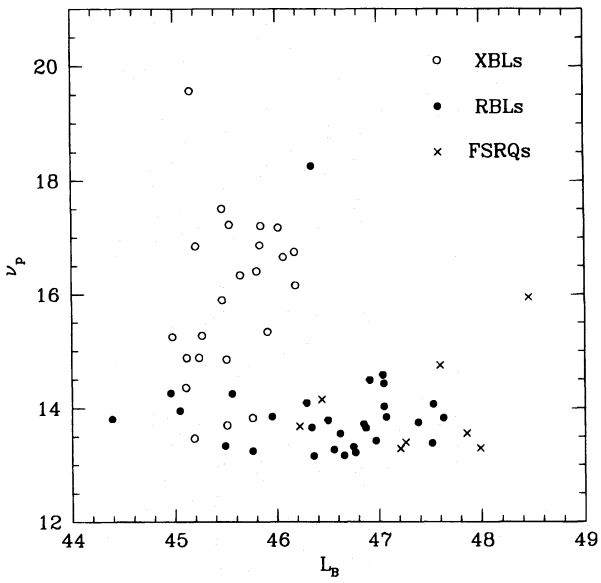

FIG. 5.—Plot of the cutoff frequency, ν_p, vs. the bolometric luminosity, L_B. Both quantity were derived from parabolic fits to the individual spectral energy distributions (see Fig. 4). More luminous sources have smaller cutoff frequencies.

as well. In summary, we examine correlations among (α_{ro}, α_{xox}, L_B) or among (α_{ro}, α_{xox}, z).

The correlation matrix for these variables is reported in Table 4A. We list the coefficients τ_{12} from Spearman nonparametric correlation analysis and the corresponding correlation probabilities in parentheses. Table 4A shows that all the variables are strongly correlated with each other.

TABLE 4A

RESULTS OF THE CORRELATION ANALYSIS: CORRELATION MATRIX

	α_{ro}	$\alpha_{ox} - \alpha_x$	z	L_B
α_{ro}	1.00	...	...	...
$\alpha_{ox} - \alpha_x$	0.527 (99.99%)	1.00	...	...
z	0.559 (99.99%)	0.291 (97.60%)	1.00	...
L_B	0.535 (99.99%)	0.355 (99.46%)	0.834 (>99.99%)	1.00

TABLE 4B

RESULTS OF THE CORRELATION ANALYSIS: PARTIAL CORRELATION

Variables 1, 2	Variable 3	$\tau_{12,3}$	P_S[a]
α_{ro}, α_{xox}	L_B	0.432	99.94%
α_{ro}, L_B	α_{xox}	0.442	99.96
α_{xox}, L_B	α_{ro}	0.097	53.77
Variables 1, 2	**Variable 3**	$\tau_{12,3}$	P_S[a]
α_{ro}, α_{xox}	z	0.468	99.98%
α_{ro}, z	α_{xox}	0.375	99.65
α_{xox}, z	α_{ro}	0.064	37.13

[a] Probability from Spearman rank correlation test that variables 1, 2 are correlated when their common dependence from variable 3 is removed, for a set of 60 data points.

In order to determine which correlation among those indicated by Table 4A is primary, i.e., not induced by a common dependence of both variables from the remaining one, we used a partial correlation test. This method consists of calculating the partial correlation coefficient $\tau_{12,3}$ associated with the probability that parameters 1 and 2 are correlated once their common dependence from a third parameter is removed, through a combination of the two-point correlation coefficients τ_{12}, τ_{13}, τ_{23} (Padovani 1992b). In Table 4B we report the coefficients $\tau_{12,3}$ for the two sets of variables (α_{ro}, α_{xox}, L_B) and (α_{ro}, α_{xox}, z). It appears that the primary correlations are between α_{ro} and α_{xox} (~99.9%), between α_{ro} and L_B (~99.9%), and α_{ro} and z (~99%), while the correlation of α_{xox} with either L_B or z is induced by the common dependence on α_{ro}. Repeating the correlation analysis with the simple X-ray slope, α_x, instead of α_{xox}, yields similar results. Again, the preferred correlations are those between the two spectral indices, α_{ro} and α_x, and between α_{ro} and L_B or z. Because of the flux-limited selections, it is not possible to distinguish the dependence on L_B from the dependence on z; in the following, we will consider the former, bearing in mind that similar results apply in the case of z.

In Figure 3*b*, α_{ro} is plotted versus L_B, illustrating together with Figure 3*a* the primary correlations governing blazar continuum emission (see also Fig. 5). Figure 3 shows that the multifrequency continua of blazars can be described by essentially one spectral parameter, either α_{ro} or α_{xox}, and that the position of the peak is linked to the luminosity. For more luminous objects, the peak of the synchrotron power occurs at lower frequencies, and the relative importance of a flat X-ray component, probably due to the inverse-Compton process, increases.

5. AVERAGE SPECTRAL ENERGY DISTRIBUTIONS OF BLAZARS

In order to illustrate the spectral properties of different blazar subclasses, we constructed average spectral energy distributions for the 1 Jy RBLs, EMSS XBLs, and S5 FSRQs, using the mean logarithmic K-corrected flux densities (the mean of the log of the values reported in Table 1). The errors of the mean were assigned as uncertainties. Figures 6*a*–6*c* shows the results for each blazar class, with the average X-ray spectrum and 1 σ (~68%) confidence range. The solid lines represent the parabolic fits to the average spectral energy distributions; the position of the peak of the parabola is marked by the arrow.

The average spectral energy distribution of the S5 FSRQs (Fig. 6*a*) shows that the optical–to–X-ray continuum is concave (i.e., the X-ray spectrum is much flatter than the optical–to–X-ray slope), and the peak in the emitted power falls in the infrared/optical range. In contrast, for the EMSS XBLs (Fig. 6*c*), the optical–to–X-ray continuum is convex (i.e., the X-ray spectrum is steeper than the optical–to–X-ray slope), and the peak of the emitted power falls in the UV/soft X-ray range. The average spectral energy distribution for the total RBL sample (Fig. 6*b*) is intermediate between the two, with the peak emission in the infrared/optical and an optical–to–X-ray continuum that could be either convex or concave.

As discussed in § 3, there is a significant spread in the spectral shapes of RBLs, with some objects having composite indices similar to XBLs and others resembling FSRQs.

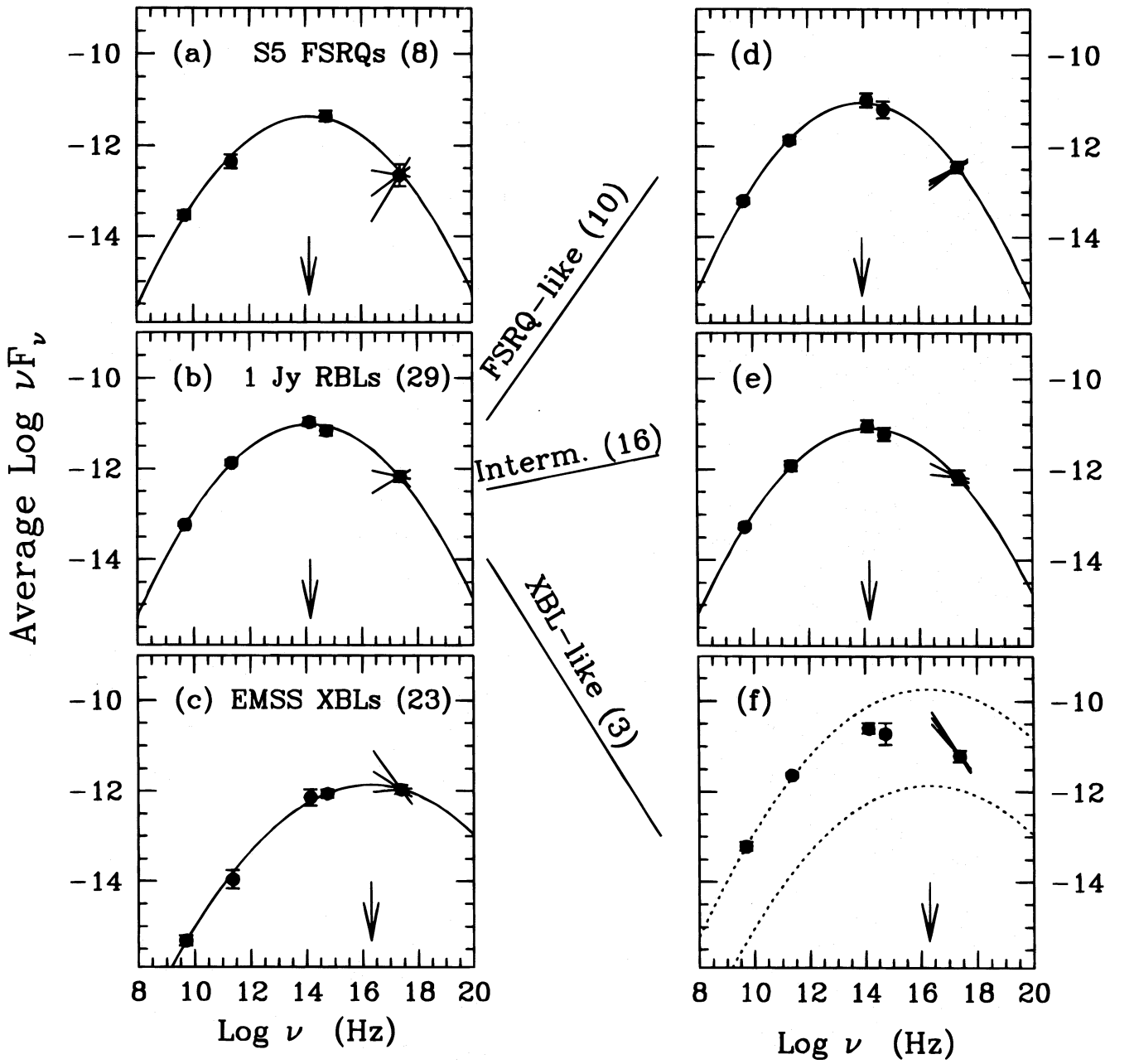

FIG. 6.—Average spectral energy distributions for (*a*) the complete sample of S5 FSRQs; (*b*) the complete sample of 1 Jy RBLs; (*c*) the complete sample of EMSS XBLs. The radio, millimeter, IR, and optical points are averages of the individual mean *K*-corrected (logarithmic) flux densities. Errors of the mean are assigned as error bars, and the *ROSAT* average index with the 1 σ ($\sim$68%) confidence range has also been plotted. The solid lines are the parabolic fits to the average spectral energy distributions; the arrow marks the position of the peak of the parabola. Going from FSRQs to RBLs to XBLs, the peak of the emission shifts toward higher energies and the mean X-ray spectrum steepens. The RBLs can be further divided into three subgroups, according to the shape of their optical–to–X-ray continua: (*d*) the subgroup of the sources with $\alpha_{xox} > 0.5$, here called FSRQ-like blazars, (*e*): the subgroup of sources with $-0.5 \lesssim \alpha_{xox} \lesssim 0.5$, which we call Intermediate, and (*f*) the subgroup of the sources with $\alpha_{xox} < -0.5$, which we call XBL-like. In panels (*d*) and (*e*) the solid lines are parabolic fits to the average spectral energy distributions. Because the subgroup of XBL-like objects contains only three sources, we did not fit a parabola to their average broadband spectrum; instead, the dashed lines in panel (*f*) represent the parabolic fit to the average spectral energy distribution of EMSS XBLs (the continuous line in panel [*c*]), renormalized to the radio and X-ray data points of the XBL-like objects.

Therefore, we also derived average spectral energy distributions for three subgroups of the RBL sample defined by the division of the concavity/convexity index at $|\alpha_{xox}| = 0.5$. This separates those RBLs with clearly concave or convex spectra from the straight or ambiguous cases, which we will call Intermediate. The average spectral energy distributions of the FSRQ-like (concave), Intermediate, and XBL-like (convex) RBLs are plotted in Figures 6*d*–6*f*. The subgroup in Figure 6*d*, or FSRQ-like objects because of the concave optical–to–X-ray spectrum, consists of the 10 1 Jy RBLs with $\alpha_{xox} > 0.5$; Figure 6*e* (Intermediate objects) includes the 16 RBLs with α_{xox} between -0.5 and $+0.5$, which is a majority of the 1 Jy RBLs; and Figure 6*f* consists of the XBL-like objects, the three RBLs with $\alpha_{xox} < -0.5$.

As before, the solid lines in Figures 6*d* and 6*e* are the parabolic fits to the average spectral energy distributions of FSRQ-like and Intermediate objects, respectively. As the XBL-like subgroup contains only three objects, we superim-

posed the parabolic fit to the average overall spectrum of the EMSS XBLs from Figure 6*c*, with a range of normalizations to match the radio and the X-ray data points, rather than fit a new parabola. While these parabolas (*dotted lines*) are not a good fit to the mean XBL-like spectrum, the position of the parabola peak matches the position of the observed peak in UV/soft X-rays, indicated in Figure 6*f* by the steep *ROSAT* spectrum.

From Figure 6*d* to Figure 6*f*, by definition the X-ray spectrum steepens, with $\langle\alpha_x\rangle$ increasing from 0.58 ± 0.32 to 1.28 ± 0.27 to 1.85 ± 0.13. The steepening of the X-ray spectrum is accompanied by a migration of the emission peak from the IR region to the UV/soft X-ray range. The average spectral properties of the three subgroups are reported in Table 3B.

We note that variability in the X-ray band can affect the shape of the optical–to–X-ray continuum, which causes the object actually to change its spectral classification. For example, 0235+164 and 0716+714, here classified as XBL-like, have X-ray spectra dominated by a steep synchrotron component in the high state, as in the present case, and by a flat Compton component when the X-ray emission fades (Madejski et al. 1996; Cappi et al. 1994). A similar case is 0537−441, which here belongs to the Intermediate group, and whose X-ray slope flattens in lower intensity states (Treves et al. 1993). It is clear that these represent transitional objects.

The position of the synchrotron peak has recently led to the introduction of a new nomenclature to designate BL Lac subclasses, based on the spectral energy distribution itself rather than the selection technique. Objects with peak synchrotron emission at lower frequencies have been called low-frequency–peaked BL Lacs, or LBLs, while objects with the peak at higher energies have been called high-frequency–peaked BL Lacs, or HBLs (Padovani & Giommi 1995, 1996). LBLs and HBLs can be divided cleanly (at present) by their relative fluxes at radio and X-ray frequencies, according to whether α_{rx} is greater or lower than 0.8, respectively. While we have characterized the differences among blazars in terms of the optical–to–X-ray continuum shape, our description of blazars as XBL-like and Intermediate/FSRQ-like is roughly equivalent to what is called HBL or LBL, respectively. This occurs because the shift in peak frequency is related to the shape of the optical–to–X-ray continuum, as discussed. The fact that some objects in the RBL sample have spectral energy distributions resembling those of XBLs and FSRQs confirms that the spectral continuity is physical rather than a function of observational uncertainties superimposed on a bifurcated classification. Although classification by spectral energy distribution should therefore be continuous as well, we use the LBL or HBL denomination as a convenient way to indicate approximately the extreme types of broadband spectra.

In conclusion, the broadband spectra of BL Lacs, either HBLs or LBLs, and of FSRQs seem to follow a systematic, continuous pattern. The power per decade has a peak in the range 10^{13}–$10^{17.5}$ Hz. When this peak is at low frequencies, $<10^{14}$ Hz, as for LBLs and FSRQs, the optical–to–X-ray continua are concave and the X-ray spectra are flat, which indicates for the X-ray emission a different origin than synchrotron radiation. These blazars also tend to be the most luminous. In contrast, HBLs have convex optical–to–X-ray continua and steep X-ray spectra consistent with a high-frequency extension of the synchrotron emission.

In order to confirm and study with more detail the continuity of blazar spectral properties, a larger sample of FSRQs observed in X-rays is clearly needed. This investigation is currently under way (Sambruna 1996).

It is interesting to note that the current samples of FSRQs are all derived from radio surveys. Based on the continuity of blazar classes, the existence of "X-ray–selected FSRQs," i.e., flat radio spectrum, emission-line blazars with $\alpha_{rx} < 0.8$, should not be expected.

6. MODELING THE CONTINUUM EMISSION FROM BLAZARS

In the following we intend to discuss how the observed spectral sequence can be interpreted on the basis of available emission models for the whole spectral energy distribution. We restrict our considerations to the synchrotron and inverse-Compton processes for the low-frequency (radio through X-rays) and for the high-frequency (X-rays through γ-rays) emission, respectively, from the same population of high-energy electrons. Possible seed photons for the inverse-Compton process are the synchrotron photons themselves (SSC; Maraschi et al. 1992), or thermal UV photons from a nearby accretion disk (Dermer, Schlickeiser, & Mastichiadis 1992) or from the broad-line emission region or ambient gas (Sikora, Begelman, & Rees 1994). The spectrum of the Compton-scattered radiation either from the synchrotron photons (self-Compton, SC) or from photons external to the jet (external Compton, EC) is tightly related to the synchrotron spectrum through the distribution of electron energies, so these models are highly constrained.

The emitted radiation is assumed to be relativistically beamed because of bulk relativistic motion of the radiating plasma. We will consider first a uniform plasma with constant particle density and magnetic field (homogeneous model). In this case, in order to reproduce the observed spectral energy distributions, the energy distribution of the radiative particles must be curved, which occurs naturally because of energy-dependent losses (Tucker 1973).

Alternatively, we will consider models in which the electron energy spectrum and magnetic field vary continuously along the direction of motion (inhomogeneous models; Ghisellini, Maraschi, & Treves 1985; Königl 1981). Homogeneous models give more insight into the role of different physical quantities but fail to fit individual spectral energy distributions in detail because of their extreme simplicity. Inhomogeneous models give good fits to the overall spectra at the expense of adding a number of parameters having to do with the largely unknown structure of the jet. In the following we discuss the selection of prototype objects, the general features of the observed overall spectra in terms of homogeneous models, and specific fits with inhomogeneous models.

6.1. *Spectral Energy Distributions of Selected Sources*

Since the γ-ray flux and spectrum are essential constraints on the inverse-Compton component, we focus on objects for which γ-ray data are available, with the additional requirement that their spectral energy distributions be representative of the average spectral energy distributions of the different classes, specifically that their positions in the $\alpha_{ro}, \alpha_{xox}$ diagram correspond to typical FSRQ-like, LBL, or HBL spectra. This gave us three 1 Jy RBLs, the objects

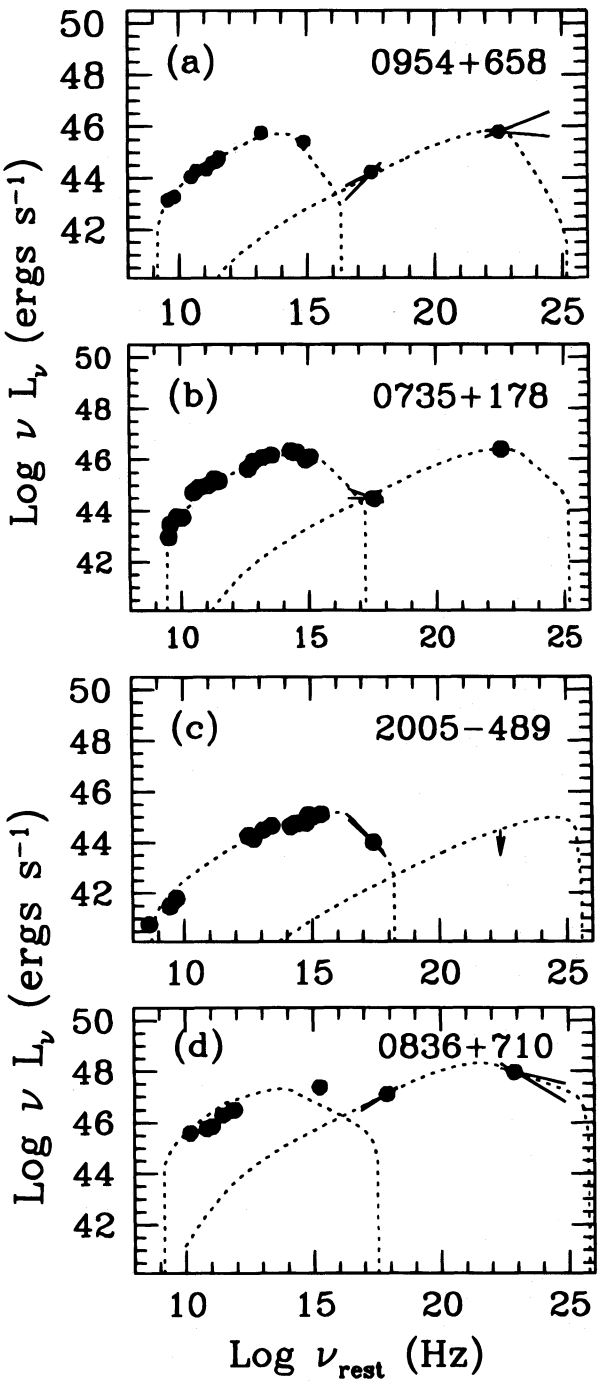

FIG. 7.—Spectral energy distributions from radio to γ-rays for three 1 Jy RBLs: (*a*) 0954+658, (*b*) 0735+168, and (*c*) 2005−489, and for the S5 FSRQ 0836+710 (*d*), which has a luminosity typical of the FSRQ class. The *ROSAT* spectra are plotted together with (nonsimultaneous) EGRET and lower frequency data. The three RBLs are representative of the three subgroups into which the 1 Jy RBL sample can be divided on the basis of the shape of the optical–to–X-ray continuum (see Fig. 6). The shapes of the spectral energy distributions of 0954+658 and 2005−489 resemble those of FSRQs and XBLs, respectively, while 0735+168 has intermediate properties. Note the increase in peak synchrotron frequencies, the steepening of the X-ray spectrum, and the shift from concave to convex optical–to–X-ray shape in going from top to bottom. The dotted lines represent fits of the (nonaccelerated) inhomogeneous jet model (Ghisellini et al. 1985), obtained with fixed viewing angle ($\theta = 7°$) and initial Lorentz factor ($\Gamma_0 = 5$); input physical parameters like the magnetic field B_0, the maximum synchrotron frequency $\nu_{\max,0}$, and the scale length R_0, are described in Table 5. Going from FSRQs to XBLs, B_0 and $\nu_{\max}$ increase and R_0 decreases; this holds independently of the exact choice of θ or Γ_0.

0954+658, 0735+178, and 2005−489 as representative FSRQ-like, LBL, and HBL, respectively.

The radio–to–γ-ray spectra of these three blazars are shown in Figures 7*a*–7*c*. From radio to UV we plot average flux densities (*filled circles*); in the X-ray band, the *ROSAT* flux is plotted together with the 90% confidence range in spectral shape (*solid lines*). For 2005−489, which had two *ROSAT* pointings, an average spectrum has been reported; in an even brighter state measured with *EXOSAT* (Sambruna et al. 1994a, b), the spectrum was flatter (see Sambruna et al. 1995 for a discussion of the broadband spectrum and spectral variability of 2005−489).

In the γ-ray EGRET band, 0954+658 was detected with good enough statistics for spectral analysis, showing a rather flat spectrum (Mukherjee et al. 1995), while 0735+178 has a 3.8 σ detection (Thompson et al. 1995). The previous 4.3 σ detection of 2005−489 (von Montigny et al. 1995) is now an upper limit (Thompson et al. 1995). The flat γ-ray spectrum for 0954+658 suggests that the peak of the emission is at even higher energies than the EGRET band, at or above 10^{24} Hz. From L_p in Table 2 and estimating the γ-ray luminosity L_C from the data in Figure 7, the ratio of power output in γ-rays to that in the radio through UV/X-ray range is $L_C/L_p \sim 3$, 1.6, and $\lesssim 0.1$ for 0954+658, 0735+178, and 2005−489, respectively.

The three spectral energy distributions in Figure 7 were chosen because, among all the objects representative of the three blazar classes, they optimized the number of data points at both low and high energies. Note that the position of the radio-to-UV emission peak in Figure 7 ranges from 10^{14} Hz to 10^{16} Hz. These do not represent extreme values for the peak frequencies, which can be as low as 10^{13} Hz and as high as 10^{18} Hz (Figs. 4 and 5). Also, their luminosities are not representative of the blazar samples, as in Table 3A, but this is not critical for fitting models as the overall spectrum scales simply. To this purpose, in Figure 7*d* we plot the radio through γ-ray spectral energy distribution of 0836+710, the only S5 FSRQ detected by EGRET (Thompson et al. 1993b). Despite the rather poor sampling and the uncertain determination of the synchrotron peak frequency, the spectrum of this object will be used to rescale the models to a higher luminosity, more typical of the FSRQ class. For 0836+710, $L_C/L_p \sim 4$.

6.2. *Homogeneous Model*

We consider synchrotron and inverse-Compton radiation (either self-Compton, SC, or external Compton, EC) produced in a region of radius R [cm] and with a constant magnetic field B [G] by a single population of relativistic electrons, with a broken power law in energy distribution, and a break point at γ_b, where γ is the Lorentz factor of the electrons (Jones, O'Dell, & Stein 1974). This is a simple approximation to the observed spectral energy distributions. For simplicity, we will neglect Klein-Nishina effects and assume the scattering takes place in the Thompson regime. If the energy spectral indices are smaller and larger than 3 below and above the break energy γ_b, respectively, the observed power per decade produced via synchrotron has a peak at a frequency

$$\nu_S = 2.8 \times 10^6 \gamma_b^2 B\delta \text{ Hz} , \quad (3)$$

where δ is the beaming factor ensuing from bulk relativistic motion of the emitting plasma (Rybicki & Lightman 1979) and is defined as $\delta = [\Gamma - (\Gamma^2 - 1)^{1/2} \cos \theta]^{-1}$, with Γ the bulk Lorentz factor of the plasma and θ the viewing angle to the jet axis. This frequency corresponds to the maximum observed power per decade of the synchrotron component (the peak of the parabolas in Fig. 4).

In this simple model, the power per decade of the Compton-scattered radiation also shows a maximum. In the case of the synchrotron self-Compton process, the maximum occurs at the (observed) frequency

$$\nu_{SC} = \tfrac{4}{3} \nu_S \gamma_b^2 \text{ Hz} , \tag{4}$$

while in the case of Compton scattering of external photons with intrinsic frequency ν_E, the maximum occurs at the observed frequency

$$\nu_{EC} = \tfrac{4}{3} \nu_E \Gamma \delta \gamma_b^2 \text{ Hz} . \tag{5}$$

Here Γ is the Lorentz factor of the plasma bulk motion. The frequencies ν_{SC} or ν_{EC} correspond to the observed peak of the γ-ray emission. From equations (3), (4), and (5) one can derive the energy of the electrons radiating at the peak as either

$$(\gamma_b^2)^{SC} = \frac{3}{4} \frac{\nu_{SC}}{\nu_S} , \tag{6}$$

or

$$(\gamma_b^2)^{EC} = \frac{3}{4} \frac{\nu_{EC}}{\nu_E \Gamma \delta} , \tag{7}$$

and the magnetic field as either

$$B^{SC} = 4.8 \times 10^{-7} \frac{\nu_S^2}{\delta \nu_{SC}} , \tag{8}$$

or

$$B^{EC} = 3.6 \times 10^{-7} \frac{\nu_S \nu_E \Gamma}{\nu_{EC}} , \tag{9}$$

as appropriate. Since $\nu_E \Gamma \delta$ is usually larger than ν_S (typical values are 10^{15} Hz for ν_E and 10 for Γ and δ), the two scenarios imply different values for γ_b and B. That is, for the same observed spectrum, an interpretation of the γ-ray peak with an SC model yields a higher electron energy and lower magnetic field than for the EC model. The differences disappear when $\nu_S \simeq \nu_E \Gamma \delta$, that is, for $\nu_S = 10^{17}$ Hz.

Let us now consider different objects along the spectral sequence as ν_S increases from 10^{13} to 10^{17} Hz. We will assume that δ and ν_E are approximately constant in different objects. Because of the lack of spectral data in the γ-ray band, we do not know at present whether ν_C (meaning ν_{SC} or ν_{EC}) increases as well. If it is constant, a larger ν_S implies a larger magnetic field in the EC model and an even larger field in the SC model. Specifically, increasing ν_S from 10^{13} Hz to 10^{17} Hz, the magnetic field increases by a factor 10^4 (EC model) or 10^8 (SC model). If, on the other hand, the ratio of the observed synchrotron and Compton peak frequencies is approximately constant in different objects, the SC model still implies increasing magnetic field and constant break energy with increasing ν_S, while the EC model yields constant magnetic field and increasing break energy of the electrons. Thus, both models imply that a systematic (though different) variation of a physical parameter, magnetic field and/or electron energy, can explain the different blazar spectra. In the case of the objects in Figure 7, assuming $\nu_C = 10^{23}$ Hz, appropriate if the spectra peak in the EGRET energy band, $\nu_S = 10^{14}$ Hz for 0954+658, 0735+178, and 0836+710, and $\nu_S = 10^{16}$ Hz for 2005−489, then $B^{SC} = 0.007$ G for 0954+658, 0735+178, and 0836+710, and 48 G for 2005−489 in the SC model; in the EC model, $B^{EC} = 4$ G for 0954+658, 0735+178, and 0836+710, and 612 G for 2005−489 (for $\delta = \Gamma = 10$).

Equation (3) also shows that, for fixed B and γ_b, and assuming a constant bulk Lorentz factor, a shift in peak frequency can be produced by an increase of δ due to a decreasing viewing angle. To reproduce the observed shift in ν_S from 10^{13} to 10^{18}, however, the beaming factor would need to vary by a factor 10^5, while estimates of δ based on SSC arguments indicate variations of at most two decades (0.1–10; Ghisellini et al. 1993). A further difficulty for this interpretation is that the peak frequency would be *higher* for smaller viewing angles, corresponding to high-power objects, contrary to the observed trend (Fig. 5).

Let L_S and L_C be the synchrotron and the Compton luminosities, respectively. In the SC model, their ratio equals the ratio of the magnetic and radiation energy densities, from which one can derive an estimate of the radius of the emitting region:

$$R = 8.1 \times 10^{-6} \frac{L_S}{B L_C^{1/2} \delta^2} \text{ cm} . \tag{10}$$

For constant δ and $L_S/L_C \gtrsim 1$, the size of the emission region increases with increasing γ-ray luminosity and decreasing magnetic field. Using the values of L_S/L_C given above, we obtain $R = 3.6 \times 10^{17}$, 1.4×10^{18}, and 3×10^{18} for 0954+658, 0735+178, and 0836+710, and 2.2×10^{14} cm for 2005−489 (for $\delta = \Gamma = 10$).

There is no equivalent to equation (10) in the EC model because the external radiation density is an unknown quantity for these three objects. One could in principle estimate the ambient EC photon density from line emission by analogy to active galactic nuclei in which a UV bump (the EC photons) and lines are both seen, but as these objects are BL Lacs, there is no real handle on the thermal photons present. Of the three RBLs discussed here, only 0954+658 has detected emission lines (Stickel, Fried, & Kühr 1993). If the energy density of external (thermal) photons increases from XBLs to RBLs to FSRQs, along with the emission-line strength, the external Compton component should become more important, as seems to be demonstrated by the EGRET blazars. A quantitative discussion of this hypothesis, however, requires a larger sample of FSRQs.

This simple discussion of homogeneous synchrotron–plus–inverse-Compton models shows that the shift in the peak of the synchrotron distribution from IR to UV frequencies requires a systematic change in the physical parameters of the emission region, in the sense of larger magnetic field and/or electron energies for the objects the energy distribution of which peaks at higher frequencies. A reliable determination of the peak of the Compton emission, a critical parameter of the model, is clearly important in order to discuss these trends in more detail.

6.3. *Inhomogeneous Jet Model*

The flat radio spectra of blazars are almost certainly caused by inhomogeneity, either of particle densities or

magnetic fields or both, in the synchrotron-emitting region (Cotton et al. 1975). Homogeneous models are a simple approximation of the emission regions of blazars. Inhomogeneous models (Ghisellini et al. 1985; Marscher & Gear 1985; Königl 1981) provide a more realistic, although still simplified, description of the structure of blazar jets. We consider here the class of inhomogeneous SSC models in which the jet geometry is represented by an inner paraboloid, responsible for the IR to soft X-ray emission, smoothly connected to an external cone, from which the radio emission arises. Along the jet, the magnetic field and particle density decrease such that $B = B_0 x^{-m}$ and $K = K_0 x^{-n}$, respectively, where $x = (R/R_0)^{\epsilon}$ is the adimensional radius of the cross section of the jet at distance R from the jet origin R_0, and $\epsilon \leq 1$. The electron spectrum has constant spectral index up to a maximum energy that decreases along the jet, and the total spectrum from the jet is the sum of the local spectra (see Ghisellini et al. 1985 for further details).

The jet plasma may accelerate outward (Ghisellini & Maraschi 1989), so that the bulk Lorentz factor of the outflowing plasma, Γ, reaches a maximum value at the end of the paraboloid ($\Gamma = \Gamma_0 x^a$). The accelerated jet model was prompted by the observational finding that RBLs are more luminous than XBLs from radio to UV (Ghisellini et al. 1986), while both classes had similar X-ray luminosity distributions (Maraschi et al. 1986). With increasing Γ, the radiation is increasingly beamed along the jet so that the net observed spectrum is a sensitive function of the viewing angle. For small viewing angles, the emission from the outer, radio-emitting part of the jet is enhanced with respect to the intrinsic, unbeamed spectrum, while the contributions from the inner, less beamed parts of the jet do not change much with the viewing angle. RBLs would thus correspond to the more aligned objects, while XBLs are seen at larger viewing angles. The number densities of the two classes also agreed nicely with this scenario (Urry et al. 1991).

A crucial test for the viewing angle hypothesis is whether it can reproduce the different spectral energy distributions observed in RBLs and XBLs (or effectively, LBLs and HBLs). Specifically, the principal observational features to reproduce are the shift of four decades in ν_p going from an LBL to an HBL and the associated change in the radio-to-optical spectral index, α_{ro}, and in the shape of the optical–to–X-ray continuum from concave to convex. Figure 8 shows examples of the angle-dependent spectral distributions produced with the accelerated jet model. The curve plotted as a solid line in Figure 8*a* represents the fit to the data of the LBL 0735+174 (Fig. 7) obtained with such model assuming an initial bulk Lorentz factor $\Gamma_0 = 1$ at the core and a final value $\Gamma_f = 10$ at the outer end of the parabolic region of the jet. The viewing angle is $\theta = 3°$. The synchrotron component has a peak at 10^{15} Hz and intersects the Compton component at $\sim 10^{17}$ Hz.

Increasing the viewing angle to 10° and 30° while holding all the other parameters fixed produces the curves shown in Figure 8*a* as dashed and dotted lines, respectively. While the luminosity of the peak (roughly proportional to the bolometric luminosity; see § 3.2) has decreased by almost 3 orders of magnitude, from $\sim 10^{46}$ ergs s^{-1} to $\sim 10^{43}$ ergs s^{-1}, thus mimicking the trend from LBLs to HBLs, the cutoff frequency has shifted forward by one to two decades

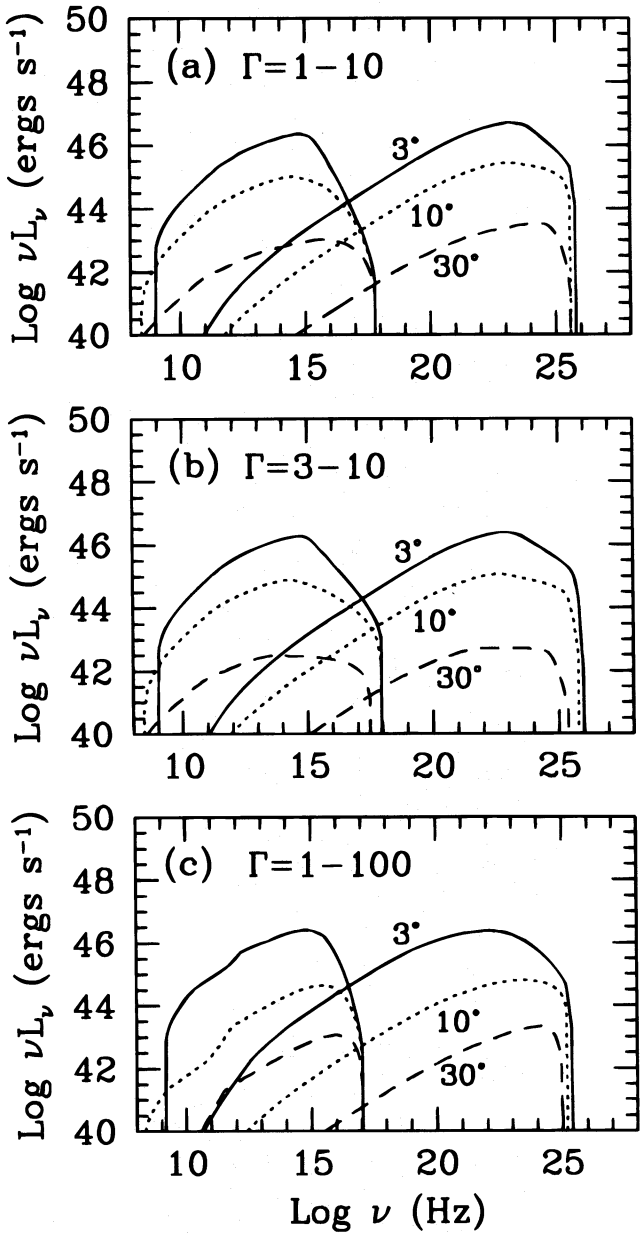

FIG. 8.—Spectral distributions from radio to γ-rays calculated with the accelerated jet model (Ghisellini & Maraschi 1989) for different viewing angles of 3° (*solid line*), 10° (*dotted line*), and 30° (*dashed line*), and different jet accelerations. In all cases, the solid line is a fit to the data of the LBL 0735+174. (*a*) Initial and final Lorentz factors $\Gamma_0 = 1$ and $\Gamma_f = 10$; (*b*) $\Gamma_0 = 5$, $\Gamma_f = 10$; (*c*) $\Gamma_0 = 1$, $\Gamma_f = 100$. In all cases, for a maximum change of the viewing angle from 3° (LBL-like) to 30° (HBL-like), the synchrotron peak frequency shifts forward only one to two decades, rather than the four needed to turn an LBL into an HBL.

in the dashed-line curve. The intersection of the synchrotron and Compton components has shifted forward to 10^{18} Hz, so that the flat spectrum does not appear until the hard X-ray range, and the soft X-ray emission is still dominated by the steep synchrotron component, which is typical of HBLs. However, while the radio–to–X-ray flux ratio decreases with increasing viewing angle, the radio-to-optical flux ratio is almost unchanged. This is still true with either weaker ($\Gamma = 3$–10) or enormously stronger ($\Gamma = 1$–100) jet acceleration, as shown in Figures 8*b* and 8*c*. Therefore, while the viewing angle model reproduces some

features in the multiwavelength colors, no choice of jet acceleration (and hence beaming collimation) can account for the observed large range in the peak frequency and the required change in α_{ro}.

Although orientation effects *alone* are not sufficient to account for the observed spectral properties of blazars, this does not imply that the average beaming factors and viewing angles of LBLs and HBLs should be the same. Indeed, the earlier considerations based on the homogeneous model suggested that the physical properties of the jets change systematically going from X-ray–selected to radio-selected sources, and the beaming factor itself may be an additional *intrinsic* difference between LBLs and HBLs.

If the Lorentz factor is constant along the jet, then the observed spectrum as a function of angle is only weakly dependent on that factor. We therefore applied inhomogeneous jet models with constant speed to fit the observed average spectral energy distributions of LBL and HBL to see how the physical parameters vary. To minimize the number of free parameters, we assumed a constant Lorentz factor $\Gamma = 5$ along the jet and fixed viewing angle $\theta = 7°$. The principal input parameters are the magnetic field, the maximum synchrotron frequency (which is proportional to the product of the magnetic field and the maximum electron energy), and the jet scale length. By varying these, we reproduced the specific spectra in Figures 7*a*–7*c*. The fitted parameter values are reported in Table 5, and the fits are shown in Figure 7 (*dotted lines*). Going from FSRQ-like to HBL spectra, there is an increase of the magnetic field B_0 by a factor 13 and of the maximum synchrotron frequency $\nu_{max,0}$ by a factor 100, while the scale length R_0 decreases by a factor of 10. In other words, the spectral sequence FSRQ-like/LBL/HBL can be explained in terms of (significant) variation of a few intrinsic parameters of the sources. The trend of the magnetic field, electron energies, and scale size is the same as in the case of the homogeneous model (§ 3.2).

Although we have not explored the parameter space exhaustively and the uncertainties on the absolute values of the parameters in Table 5 are likely large (due to the fact that the model is underconstrained), the trend of their variation from one object to another is not ambiguous. A different choice of viewing angle and/or Lorentz factor yields other values of B_0, ν_{max}, and R_0, but still the magnetic field and ν_{max} are observed to increase and the scale size to decrease from FSRQ-like to LBLs to HBLs.

The fit to the higher luminosity spectrum of 0836+710, which is otherwise similar in shape to the spectrum of 0954+658, requires a further increase of the scale length and a decrease of the magnetic field with respect to the latter object (Table 5), which confirms the mentioned trends of these parameters.

Note in Figure 7 that the synchrotron self-Compton emission is insufficient in reproducing the flat γ-ray spectrum of 0954+658. A peak at much higher γ-ray frequencies than predicted by the model is indicated for the Compton component. It is possible, as suggested earlier (Comastri et al. 1995), that contributions to the γ-rays from an external radiation field are present for this object.

In conclusion, we have shown that orientation effects alone are not sufficient to turn an HBL into an LBL. Instead, the full range of observed spectral energy distributions can be accounted for by a change of intrinsic physical parameters. The magnetic field and/or the critical electron energy should decrease and the size of the emission region should increase with increasing luminosity going from an HBL to an LBL. The fact that the highest luminosity blazars show emission lines may suggest that photons external to the jet can play a more important role in more luminous objects.

7. SUMMARY AND DISCUSSION

We have compared the continuum emission properties of three complete blazar samples, systematically observed in soft X-rays with the *ROSAT* PSPC, specifically, the radio-selected BL Lacs from the 1 Jy radio catalog, the X-ray–selected BL Lacs from the X-ray EMSS survey, and the flat spectrum radio quasars from the S5 radio survey. Our principal conclusions are as follows.

1. Considering the two-point spectral indices α_{rx}, α_{ro}, and α_{ox}, we find that XBLs are statistically well separated from both RBLs and FSRQs, having flatter (lower) indices in all bands, whereas these indices do not distinguish FSRQs from RBLs. However, using the measured spectral index in the X-ray band together with α_{ox} to describe the concavity or convexity of the optical–to–X-ray continuum via $\alpha_{xox} = \alpha_{ox} - \alpha_x$, the three groups can be separated clearly. The optical–to–X-ray continua are generally convex for XBLs ($\alpha_{xox} < 0$), concave for FSRQs ($\alpha_{xox} > 0$), and intermediate for RBLs ($\alpha_{xox} \sim 0$).

2. XBLs, RBLs, and FSRQs can be arranged in a continuous spectral sequence in a color-color diagram, suggesting that similar physical processes operate in all objects under a range of intrinsic physical conditions or beaming param-

TABLE 5

INHOMOGENEOUS JET MODELS

Parameter	0954+658 FSRQ-like (LBL)	0735+168 Intermediate (LBL)	2005−489 XBL-like (HBL)	0836+710 S5 FSRQ	Notes
B_0	6	40	80	4	[G], initial magnetic field
$\nu_{max,0}$	4×10^{15}	3×10^{16}	3×10^{17}	5×10^{16}	[Hz], initial maximum synchrotron frequency
R_0	1.1×10^{15}	5×10^{14}	1×10^{14}	6×10^{15}	[cm], initial radius of paraboloid
$R_{max,par}$	1.2×10^{18}	5×10^{17}	1×10^{17}	6.6×10^{18}	[cm], maximum length of paraboloid
$R_{max,cone}$	5.5×10^{21}	2.5×10^{20}	3×10^{20}	3×10^{21}	[cm], maximum length of cone
K_0	2.2×10^4	8.3×10^4	6.8×10^4	2×10^4	[cm^{-3}], initial particle density
Γ_0	5	5	5	5	Initial bulk Lorentz factor
θ	7°	7°	7°	7°	Viewing angle
m	1.0	1.0	1.0	1.0	$B = B_0(r/r_0)^{-m}$
η	0.6	0.7	0.65	1.1	$\nu_{max} = \nu_{max,0}(r/r_0)^{-\eta}$
n	0.3	0.5	0.5	0.3	$K = K_0(r/r_0)^{-n}$

eters. The indices α_{ro} and α_{xox} are strongly correlated, in the sense that higher α_{ro} (lower peak frequency) is associated with larger α_{xox} (more concave optical–to–X-ray spectrum), so to first order blazar broadband spectra can be characterized by either index.

3. A partial correlation analysis indicates that the radio-to-optical spectral index, α_{ro}, correlates with the concavity/convexity spectral index, α_{xox}, and with the (apparent) bolometric luminosities and with redshift. It is not possible to separate the dependence on luminosity from the dependence on redshift because of the flux-limited selection of the three samples.

4. We demonstrated the spectral continuity of FSRQs, RBLs, and XBLs with average overall spectra for each sample. These showed that the peak in the power per decade shifts to higher frequency with decreasing luminosity, while the optical–to–X-ray continuum changes from concave ($\alpha_x < \alpha_{ox}$) to convex ($\alpha_x > \alpha_{ox}$). It is possible to divide the RBL sample into three subgroups on the basis of the α_{xox} index into FSRQ-like, XBL-like, and Intermediate RBLs; the spectral continuity within the RBL sample itself further emphasizes the common underlying physics among all blazars.

5. The observed sequence in the shapes of blazar spectral energy distributions can not be accounted for by the sole change of viewing angle. It requires instead a smooth change of intrinsic physical parameters. Specifically, the transition XBL-like/RBL-like/FSRQ-like corresponds to decreasing magnetic densities and/or decreasing electron densities. An independent parameter difficult to quantify here is the energy density of the external photons, which may play an important role in the inverse-Compton process, particularly in FSRQ-like blazars.

The continuity in the spectral energy distributions of blazars points toward an underlying commonality, in the sense that, from the point of view of their continuum emission, blazars form a unique population with the same emission processes operating under a range of physical conditions. The different local surroundings, which give rise to emission lines of different strength in different blazar subclasses, may be associated with, or be responsible for, the changing physical conditions. In fact, the sequence defined in the color-shape diagram in Figure 3*a* roughly corresponds to increasing importance of emission lines. It is possible that the flatter X-ray slopes of FSRQs with respect to RBLs are related to an increasing contribution of the external Compton scattering of thermal photons from the broad-line region and/or an accretion disk. In this case we would expect a strong correlation between the shape of the X-ray continuum and the luminosity or equivalent width of the emission lines. However, we can not exclude that we observe harder X-ray spectra in FSRQs as a result of the presence of intrinsic absorption or/and a more complex spectral shape (Elvis et al. 1994; Serlemitsos et al. 1994). Future simultaneous optical, UV, and X-ray (*ASCA*, *XTE*) spectroscopy of a larger sample of emission-line blazars would help in clarifying these points.

Our correlation analysis indicates that it is possible to describe the spectral sequence in terms of a single parameter (to first order) such as the luminosity. Since there are reliable indications that the average beaming factor for different kinds of blazars are not widely different (Ghisellini et al. 1993), the apparent luminosity is, on average, related to the intrinsic power dissipated in the jet. According to our interpretation of the spectral sequence in terms of homogeneous and inhomogeneous SSC models, more powerful jets would have lower magnetic fields and/or lower particle energies and larger emission regions than low-power jets. This could be understood either as a scale effect, perhaps if more powerful sources had larger masses of the central black hole, or as a physical effect associated with the distance at which the power of the jet is (partially) converted into radiation. The matter surrounding the jet may play a role in the process of conversion of energy into radiation. We recall that the morphology of the extended radio emission, which is also associated with the power of the source, may also depend on such interaction (De Young 1993; Bicknell et al. 1990). The latter picture is consistent with a unified model of blazars whereby relativistic jets are present in the cores of both FR I and FR II galaxies (Maraschi & Rovetti 1995). Although we discuss the correlation of spectral parameters with luminosity, evolutionary effects can not be excluded. They could operate as in other types of quasars by changing the "typical" or average luminosity with time.

The continuous spread of peak frequencies observed within blazars has led to a new physical classification of the different subclasses into LBLs and HBLs. The observed range of peak frequencies is from 10^{13} to 10^{18} Hz. Values of ν_p lower than 10^{13} Hz are unlikely since the self-absorption process becomes important at lower frequencies. Objects with cutoff frequencies higher than 10^{18} Hz would be detected only in hard X-ray surveys but should be faint at lower frequencies, which would make their discovery difficult.

In conclusion, the family of blazars is well understood as a phenomenon related to the presence of a relativistic jet, with radiation emitted via synchrotron and Compton-scattering mechanisms. Using existing multifrequency data we showed that blazar classes have different but continuous spectral properties, and we ruled out the viewing angle hypothesis as the sole difference between RBLs and XBLs. This study is limited by the lack of simultaneous data from radio to γ-rays. To make further progress, it is crucial to obtain simultaneous measurements from radio to γ-rays, especially with an accurate determination of the positions of the synchrotron and γ-ray peaks, since these quantities are linked to important physical parameters of the source such as dimension and magnetic field. Multifrequency monitoring of a large sample of emission-line blazars would provide definitive analysis of continuum properties and would make clear the relative importance of self-Compton and external Compton scattering mechanisms.

We are grateful to Gabriele Ghisellini for providing his code of the inhomogeneous jet model and for a critical reading of the manuscript which yielded several useful comments. We also thank the referee for a thoughtful report and John Stocke for interesting conversations. R. M. S. acknowledges financial support from NASA grants NAG 5-1918 and NAG 5-2510 while at STScI.

APPENDIX A

The following table, Table A1, lists the references to the individual radio, millimeter, IR, and optical flux densities for the EMSS XBLs, 1 Jy RBLS, and S5 FSRQs. These data were collected from the literature in the period 1980–early 1995, except for the radio, where most measurements were done at earlier epochs. The average fluxes and dispersions, which were used to construct the multifrequency energy distributions of the three blazar samples (see § 2), are reported in Table 1.

TABLE A1

REFERENCES FOR TABLE 1

Object	Radio (5 GHz)	Millimeter (230 GHz)	IR (2.2 μm)	Optical (5500 Å)
		EMSS XBLs		
0122.1+0903.....	1	...	2	1, 3
0158.5+0019.....	1	...	...	1, 3
0205.7+3509.....	1	...	2	1, 3
0257.9+3429.....	1	...	2	1, 3
0317.0+1834.....	1	...	2	1, 3, 4, 5, 6
0419.3+1943.....	1	...	2	1
0607.9+7108.....	1	...	...	1
0737.9+7441.....	1	...	...	1
0922.9+7459.....	1	...	...	1, 3
0950.9+4929.....	1	...	2	1, 3
1019.0+5139.....	1	...	...	1
1207.9+3945.....	1	...	2	1
1221.8+2452.....	1	7	2	1, 3
1229.2+6430.....	1	7	...	1, 3
1235.4+6315.....	1	...	...	1, 3, 4
1402.3+0416.....	1	7	2, 8, 9	1, 3, 8
1407.9+5954.....	1	7	2	1, 3
1443.5+6349.....	1	7	...	1
1458.8+2249.....	1	...	2	1, 3
1534.8+0148.....	1	7	2	1, 3
1552.1+2020.....	1	...	2	1, 3
1757.7+7034.....	1	...	...	1
2143.3+0704.....	1	7	2	1, 3
		1 Jy RBLs		
0048−097	1, 2, 3	4, 5	6, 7, 8, 9, 10, 11	6, 8, 12, 13, 14
0118−272	1	5	6, 7, 8, 9, 15	6, 8, 15, 16
0235+164	1, 2, 3, 17, 18, 19, 20–27	4, 5, 26, 28	8, 9, 18, 28, 29, 30–35	14, 30, 35–40
0426−380	1, 41	...	...	42
0454+844	1, 5, 20, 43, 44	5	...	14, 45
0537−441	1, 17, 46	...	6, 7, 9, 47, 48	6, 12, 16, 48–50
0716+714	1, 17, 27, 43	4, 5	35	14
0735+178	1–3, 18–27, 51–54	4, 5	6, 9, 10, 12, 18, 28–35, 54–56	6, 8, 12, 14, 30, 35–39, 54, 56–40, 60–64
0814+425	1, 19, 20, 25, 65	4, 5	29	14, 45
0851+202	1, 18, 19, 25–27	1, 4, 5, 26, 28	6–9, 18, 28–30, 32–35, 38, 54, 55, 66–68	6, 8, 12, 30, 34–40, 57–59, 61–64, 69–74
0954+658	19, 20, 27, 65	4, 26	...	14, 75, 76
1144−379	1	...	6, 7	6, 16, 77
1147+245	1, 2, 3, 25	4, 26	29, 32, 78	8, 14, 40, 76
1308+326	1–3, 18–20, 25–27, 54, 65, 79	4, 5, 26	18, 28–30, 32–35, 54, 55	30, 34–36, 54, 80, 81
1418+546	1, 2, 19, 20, 25, 54	4, 5, 26	8, 29, 30, 32–35, 38, 54, 83	8, 14, 30, 34, 36, 54, 57, 58
1519−273	1, 20	5	29	16
1538+149	1–3, 24, 25, 54, 65	4, 26	6, 7, 9, 15, 29, 32, 54	6, 12, 14, 15, 54
1652+398	1–3, 19, 20, 25–27, 65, 83–85	4, 26	29, 34, 38, 86–88	34, 37, 39, 57, 58, 75, 89, 90
1749+096	1–3, 19, 20, 22, 26, 54	4, 5, 26	6, 7, 9, 29, 30, 32, 35, 54, 55	6, 8, 12, 14, 54, 64
1749+701	3, 5, 19, 20, 21, 26, 27, 43, 53	5, 26	...	14, 45, 75
1803+784	1, 20, 26, 27, 43, 91	4, 5, 26	92	14, 45, 75
1807+698	1, 2, 23, 25, 26, 53, 54, 91, 93	4, 5, 26	35, 48, 94	54, 58, 59, 75, 94
1823+568	1, 19, 26, 53, 91	4, 5, 26	29	42
2005−489	1, 95	...	6, 7	6, 95, 96
2007+777	1, 20, 26, 43	4, 26	...	14, 20, 45
2131−021	1, 20	5	29	20, 45, 76
2200+420	1–3, 18–23, 26, 27, 65, 91, 97	4, 5, 26	8, 9, 18, 28, 30, 32–35, 38, 92, 98, 99	8, 14, 30, 39, 61, 69, 100, 101
2240−260	1	...	6, 7, 9, 29	6, 16, 77
2254+074	2, 3, 20, 23–25	5	6, 7, 9, 29	6, 8, 12, 14, 45, 63, 70, 77

TABLE A1—*Continued*

Object	Radio (5 GHz)	Millimeter (230 GHz)	IR (2.2 μm)	Optical (5500 Å)
		S5 FSRQs		
0016+731.....	1, 2	3, 4	...	5
0153+744.....	1, 2	3	...	5
0212+735.....	1, 2	3, 6	...	5
0615+820.....	1	3	...	5
0836+710.....	1, 2	3, 4	...	5
1039+811.....	1, 2	3, 6	...	5
1150+812.....	1, 2	3,	...	5
1928+738.....	1, 2	3, 6	...	5

REFERENCES FOR THE EMSS XBLs—(1) Stocke et al. 1991; (2) Gear 1993a; (3) Jannuzi, Smith, & Elston 1993; (4) Xie et al. 1988a; (5) Xie et al. 1990; (6) Xie et al. 1991; (7) Gear 1993b; (8) Falomo et al. 1993a; (9) Bersanelli et al. 1992.

REFERENCES FOR THE 1 Jy RBLs—(1) Kühr et al. 1981; (2) Antonucci & Ulvestad 1985; (3) Weiler & Johnston 1980; (4) Steppe et al. 1992; (5) Steppe et al. 1988; (6) Falomo et al. 1993a; (7) Bersanelli et al. 1992; (8) Mead et al. 1990; (9) Allen, Ward, & Hyland 1982; (10) Lepine, Braz, & Epchtein 1985; (11) Wright, Ables, & Allen 1983; (12) Brindle et al. 1986; (13) Falomo et al. 1989; (14) Wills et al. 1992; (15) Falomo et al. 1993b; (16) Impey & Tapia 1990; (17) Henri, Pelletier, & Roland 1993; (18) Brown et al. 1986; (19) Rudnick et al. 1985; (20) Argue et al. 1984; (21) Bääth et al. 1981; (22) Jones et al. 1981; (23) Ryle, O'Dell, & Waggett 1975; (24) Bennett et al. 1986; (25) Owen et al. 1980; (26) Gear et al. 1994; (27) Quirrenbach et al. 1992; (28) Gear et al. 1986a; (29) Gear 1993a; (30) Smith et al. 1987; (31) Gear et al. 1985; (32) Impey et al. 1984; (33) Holmes et al. 1984; (34) Sitko et al. 1983; (35) Sitko & Sitko 1991; (36) Sitko, Schmidt, & Stein 1985; (37) Sillanpää, Mikkola, & Valtaoja 1991; (38) Takalo et al. 1992; (39) Sillanpää, Haarala, & Korhonen 1988; (40) Moles, Garcia-Pelayo, & Masegosa 1984; (41) Quiniento, Cerosimo, & Colomb 1988; (42) Stickel et al. 1991; (43) Eckart et al. 1987; (44) Impey, Lawrence, & Tapia 1991; (45) Kühr & Schmidt 1989; (46) Robertson et al. 1993; (47) Tanzi et al. 1986; (48) Cruz-Gonzalez & Huchra 1984; (49) Adam 1985; (50) Hamuy & Maza 1987; (51) Bääth & Zhang 1991; (52) Gabuzda et al. 1989; (53) O'Dea, Barvainis, & Challis 1988; (54) Landau et al. 1986; (55) Roellig et al. 1986; (56) Bregman et al. 1984; (57) Takalo 1991; (58) Valtaoja et al. 1991; (59) Webb et al. 1988; (60) Valtaoja et al. 1993; (61) Xie et al. 1988a; (62) Xie et al. 1987; (63) Xie et al. 1990; (64) Xie et al. 1991; (65) Zensus, Porcas, & Pauliny-Toth 1984; (66) Gear, Robson, & Brown 1986b; (67) Sitko & Junkarinen 1985; (68) Lorenzetti et al. 1989; (69) Carini et al. 1992; (70) Moles et al. 1985; (71) Smith, Allen, & Angel 1993; (72) Takalo et al. 1990; (73) Weistrop et al. 1985; (74) Sillanpää et al. 1985; (76) Burbidge & Hewitt 1987; (77) Falomo et al. 1994; (78) Lorenzetti et al. 1990; (79) Rogora, Padrielli, & de Ruiter 1987; (80) Sitko et al. 1984; (81) Moore & Stockman 1984; (82) Worrall et al. 1984a; (83) Giovannini, Feretti, & Comoretto 1990; (84) van Breugel & Schilizzi 1986; (85) Kojoian et al. 1980; (86) Kidger, Takalo, & De Diego 1992; (87) Impey 1983; (88) Koitilanen et al. 1992; (89) Moles, Masegosa & del Olmo 1987; (90) Jannuzi et al. 1993; (91) Pearson & Readhead 1988; (92) Heckman et al. 1983; (93) van Bruegel et al. 1981; (94) Worrall et al. 1984b; (95) Wall et al. 1986; (96) Falomo et al. 1987; (97) Ulvestad & Johnston 1984; (98) Kawaii et al. 1991; (99) Bregman et al. 1990; (100) Xie et al. 1988b; (101) Doroshenko et al. 1986.

REFERENCES FOR THE S5 FSRQs—(1) Kühr et al. 1981; (2) Eckart et al. 1987; (3) Steppe et al. 1988; (4) Bloom et al. 1994; (5) Véron-Cetty & Véron 1992; (6) Steppe et al. 1992.

REFERENCES

Adam, G. 1985, A&AS, 61, 225
Allen, D. A., Ward, M. J., & Hyland, A. R. 1982, MNRAS, 199, 969
Antonucci, R. R. J., & Ulvestad, J. S. 1985, ApJ, 294, 158
Argue, A. N., et al. 1984, A&A, 130, 191
Bääth, L. B., & Zhang, F. J. 1991, A&A, 243, 328
Bääth, L. B., et al. 1981, A&A, 96, 316
Bennett, C. L., Lawrence, C. R., Burke, B. F., Hewitt, J. N., & Mahoney, J. 1986, ApJS, 61, 1
Bersanelli, M., Bouchet, P., Falomo, R., & Tanzi, E. G. 1992, AJ, 104, 28
Biermann, P., et al. 1981, ApJ, 247, 53
Bicknell, G. V., de Ruiter, H. R., Fanti, R., Morganti, R., & Parma, P. 1990, ApJ, 354, 98
Bloom, S. D., Marscher, A. P., Gear, W. K., Teräsranta, H., Valtoja, E., Aller, H. D., & Aller, M. F. 1994, AJ, 108, 398
Bregman, J. N., et al. 1990, ApJ, 352, 574
Bregman, J. N., Maraschi, L., & Urry, C. M. 1987, in Scientific Accomplishments of *IUE*, ed. Y. Kondo (Dordrecht: Reidel), 685
Bregman, J. N., et al. 1984, ApJ, 276, 454
Brindle, C., Hough, J. H., Bailey, J. A., Axon, D. J., & Hyland, A. R. 1986, MNRAS, 221, 739
Brown, L. M. J., et al. 1989, ApJ, 340, 129
Brunner, H., Lamer, G., Worrall, D. M., & Staubert, R. 1994, A&A, 287, 436
Burbidge, G., & Hewitt, A. 1987, AJ, 93, 1
Cappi, M., Comastri, A., Molendi, S., Palumbo, G. G. C., Della Ceca, R., & Maccacaro, T. 1995, MNRAS, 271, 438
Cardelli, J. A., Clayton, G. C., & Mathis, J. S. 1989, ApJ, 345, 245
Carini, M. T., Miller, H. R., Noble, J. C., & Goodrich, B. D. 1992, AJ, 104, 15
Celotti, A., Maraschi, L., Ghisellini, G., Caccianiga, A., & Maccacaro, T. 1993, ApJ, 416, 118
Celotti, A., Maraschi, L., & Treves, A. 1991, ApJ, 377, 403
Comastri, A., Molendi, S., & Ghisellini, G. 1995, MNRAS, 277, 297
Cotton, W. D., et al. 1975, ApJ, 238, L23
Cruz-Gonzalez, I., & Huchra, J. P. 1984, AJ, 89, 441
Della Ceca, R., Palumbo, G. G. C., Persic, M., Boldt, E. A., De Zotti, G., & Marshall, E. E. 1990, ApJS, 72, 471
Dermer, C. D., & Gehrels, N. 1995, ApJ, 447, 103
Dermer, C. D., Schlickeiser, R., & Mastichiadis, A. 1992, A&A, 256, L27
De Young, D. S. 1993, ApJ, 405, L13
Dondi, L., & Ghisellini, G. 1995, MNRAS, 273, 583
Doroshenko, V. T., et al. 1986, A&A, 321, 325
Eckart, A., Witzel, A., Biermann, P., Johnston, K. J., Simon, R., Schalinski, C., & Kühr, H. 1987, A&A, 168, 17
Elvis, M., Fiore, F., Wilkes, B., McDowell, J., & Bechtold, J. 1994, ApJ, 422, 60
Elvis, M., Lockman, F. J., & Wilkes, B. J. 1989, AJ, 97, 777
Falomo, R., Bersanelli, M., Bouchet, P., & Tanzi, E. G. 1993a, AJ, 106, 11
Falomo, R., Bouchet, P., Maraschi, L., Tanzi, E. G., & Treves, A. 1989, ApJ, 335, 122
Falomo, R., Maraschi, L., Tanzi, E. G., & Treves, A. 1987, ApJ, 318, L39
Falomo, R., Scarpa, R., & Bersanelli, M. 1994, ApJS, 93, 125
Falomo, R., Treves, A., Chiappetti, L., Maraschi, L., Pian, E., & Tanzi, E.G. 1993b, ApJ, 402, 532
Gabuzda, D. C., Cawthorne, T. V., Roberts, D. H., & Wardle, J. F. C. 1989, ApJ, 347, 701
Gear, W. K. 1993a, MNRAS, 264, 919
———. 1993b, MNRAS, 264, L21
Gear, W. K. et al. 1986a, ApJ, 304, 295
Gear, W. K., Robson, E. I., & Brown, L. M. J. 1986b, 324, 546
Gear, W. K., et al. 1985, ApJ, 291, 511
Gear, W. K., et al. 1994, MNRAS, 267, 167
Ghisellini, G., & Maraschi, L. 1989, ApJ, 340, 181
Ghisellini, G., Maraschi, L., Tanzi, E. G., & Treves, A. 1986, ApJ, 310, 317
Ghisellini, G., Maraschi, L., & Treves, A. 1985, A&A, 146, 204
Giommi, P., Ansari, S. G., & Micol, A. 1995, A&AS, 109, 267
Ghisellini, G., Padovani, P., Celotti, A., & Maraschi, L. 1993, ApJ, 407, 65
Giommi, P., Barr, P., Garilli, B., Gioia, I. M., & Maccacaro, T. 1987, ApJ, 322, 662
Giommi, P., & Padovani, P. 1994, MNRAS, 268, L51
Giovannini, G., Feretti, L., & Comoretto, G. 1990, ApJ, 358, 159
Hamuy, M., & Maza, J. 1987, A&AS, 68, 383
Heckman, T. M., Lebofsky, M. J., Rieke, G. H., & van Breugel, W. 1983, ApJ, 272, 400
Henri, G., Pelletier, G., & Roland, J. 1993, ApJ, 404, L41
Holmes, P. A., Brand, P. W. J. L., Impey, C. D., & Williams, P. M. 1984, MNRAS, 210, 691
Hunter, S. D., et al. 1993, A&A, 272, 59
Impey, C. D. 1983, MNRAS, 202, 397
Impey, C. D., Brand, P. W. J. L., Wolstencroft, R. D., & Williams, P. M. 1984, MNRAS, 209, 245
Impey, C. D., Lawrence, C. R., & Tapia, S. 1991, ApJ, 375, 46
Impey, C. D. & Neugebauer, G. 1988, AJ, 95, 307
Impey, C. D. & Tapia, S. 1988, ApJ, 333, 666
Jannuzi, B. T., Smith, P. S., & Elston, R. 1993, ApJS, 85, 265
———. 1994, ApJ, 428, 130
Jones, T. W., O'Dell, S. L., & Stein, W. A. 1974, ApJ, 188, 353
Jones, T. W., Rudnick, L., Owen, F. N., Puschell, J. J., Ennis, D. J., & Werner, M. W. 1981, ApJ, 243, 97
Kawai, M., et al. 1991, ApJ, 382, 508
Kidger, M. R., Takalo, L., & De Diego, J. A. 1992, A&A, 254, 65

Königl, A. 1981, ApJ, 243, 700
Kojoian, G., Tovmassian, H. M., Dickinson, D. F., & StClaire Dinger, A. 1980, AJ, 85, 1462
Kotilainen, J. K., Ward, M. J., Boisson, C., DePoy, D. L., & Smith, M. G. 1992, MNRAS, 256, 149
Kühr, H., & Schmidt, G. D. 1990, AJ, 99, 1
Kühr, H., Witzel, A., Pauliny-Toth, I. I. K., & Nauber, U. 1981, A&AS, 45, 367
Landau, R., et al. 1986, ApJ, 308, 78
Ledden, J. E. & O'Dell, S. L. 1985, ApJ, 298, 630
Lepine, J. R. D., Braz, M. A., & Epchtein, N. 1985, A&A, 149, 351
Lorenzetti, D., Massaro, E., Perola, G. C., & Spinoglio, L. 1989, ApJS, 71, 175
———. 1990, A&A, 235, 35
Maccagni, D., & Tarenghi, M. 1981, ApJ, 243, 42
Madejski, G., Takahashi, T., Tashiro, M., Kubo, H., Hartman, R., Kallman, T., & Sikora, M. 1996, ApJ, 459, 156
Maraschi, L., et al. 1994, ApJ, 435, L91
Maraschi, L., Ghisellini, G., & Celotti, A. 1992, ApJ, 397, L5
Maraschi, L., Ghisellini, G., Tanzi, E. G., & Treves, A. 1986, ApJ, 310, 325
Maraschi, L., & Rovetti, F. 1994, ApJ, 436, 79
Marscher, A. P. & Gear, W. K. 1985, ApJ, 298, 114
Mead, A. R. G., Ballard, K. R., Brand, P. W. J. L., Hough, J. H., Brindle, C., & Bailey, J. A. 1990, A&AS, 83, 183
Moles, M., Garcia-Pelayo, J., & Masegosa, J. 1984, MNRAS, 211, 621
Moles, M., Garcia-Pelayo, J. M., Masegosa, J., & Aparicio, A. 1985, ApJS, 58, 255
Moles, M., Masegosa, J., & del Olmo, A. 1987, AJ, 94, 1143
Moore, R. L., & Stockman, H. S. 1984, ApJ, 279, 465
Morris, S. L., Stocke, J. T., Gioia, I. M., Schild, R. E., Wolter, A., Maccacaro, T., & Della Ceca, R. 1991, ApJ, 380, 49
Mukherjee, R., et al. 1995, ApJ, 445, 189
Mushotzky, R. F., Boldt, E. A., Holt, S. S., Serlemitsos, P. J., Swank, J. H., Rothschild, R. H., & Pravdo, S. H. 1978, ApJ, 226, 65
O'Dea, C. P., Barvainis, R., & Challis, P. M. 1988, AJ, 96, 435
Owen, F. N., Spangler, R., & Cotton, W. D. 1980, AJ, 85, 351
Padovani, P. 1992a, MNRAS, 257, 404
———. 1992b, A&A, 256, 399
Padovani, P., & Giommi, P. 1995, ApJ, 444, 567
———. 1996, MNRAS, submitted
Pearson, T. J., & Readhead, A. C. S. 1988, ApJ, 328, 114
Perlman, E. S., et al. 1996a, ApJ, in press
Perlman, E. S., Stocke, J. T., Wang, Q. D., & Morris, S. L. 1996b, ApJ, 456, 451
Pian, E., & Treves, A. 1993, ApJ, 416, 130
Quiniento, Z. M., Cersosimo, J. C., & Colomb, F. R. 1988, A&AS, 76, 21
Quirrenbach, A., et al. 1992, A&A, 258, 279
Rieke, G. H., & Lebofsky, M. 1985, ApJ, 288, 618
Roellig, T. L., Becklin, E. E., Impey, C. D., & Werner, M. W. 1986, ApJ, 304, 646
Robertson, D. S., et al. 1993, AJ, 105, 353
Rogora, A., Padrielli, L., & de Ruiter, H. R. 1987, A&AS, 67, 267
Rybicki, G., & Lightman, A. 1979, Radiation Processes in Astrophysics (New York: Wiley)
Ryle, M., O'Dell, D. M., & Waggett, P. C. 1975, MNRAS, 173, 9
Rudnick, L., et al. 1985, ApJS, 57, 693
Sambruna, R. M. 1996, in preparation
Sambruna, R. M., Barr, P., Giommi, P., Maraschi, L., Tagliaferri, G., & Treves, A. 1994a, ApJ, 434, 468
———. 1994b, ApJS, 95, 371
Sambruna, R. M., Urry, C. M., Ghisellini, G., & Maraschi, L. 1995, ApJ, 449, 567
Schachter, J. F., et al. 1993, ApJ, 412, 541
Schwartz, D. A., Brissenden, R. J. V., Tuhoy, I. R., Feigelson, E. D., Hertz, P. L., & Remillard, R. A. 1989, in BL Lac Objects, ed. L. Maraschi, T. Maccacaro, & M.-H. Ulrich (Berlin: Springer), 209
Schwartz, D. A., Griffiths, R. E., Schwarz, J., Doxsey, R. E., & Johnston, M. D. 1979, ApJ, 229, 53
Serlemitsos, P., Yaqoob, T., Ricker, G., Woo, J., Kunieda, H., Terashima, Y., & Ywasawa, K. 1994, PASJ, 46, L43
Shull, J. M., & Van Steenberg, M. E. 1985, ApJ, 294, 599
Sikora, M., Begelman, M. C., & Rees, M. J. 1994, ApJ, 421, 153
Sillanpää, A., Haarala, S., & Korhonen, T. 1988, A&AS, 72, 347
Sillanpää, A., Mikkola, S., & Valtaoja, L. 1991, A&AS, 88, 225
Sillanpää, A., Teerikorpi, P., Haarala, S., Korhonen, T., Efimov, Y. S., & Shakhovskoy, N. M. 1985, A&A, 147, 67
Sitko, M. L. & Junkarinen, V. T. 1985, PASP, 97, 1158
Sitko, M. L., & Sitko, A. K. 1991, PASP, 103, 160
Sitko, M. L., Schmidt, G. D., & Stein, W. A. 1985, ApJS, 59, 323
Sitko, M. L., Stein, W. A., & Schmidt, G. D. 1984, ApJ, 282, 29
Sitko, M. L., Stein, W. A., Zhang, Y. X., & Wisńiewski, W. Z. 1983, PASP, 95, 724
Smith, P. S., Allen, R. G., & Angel, J. R. P. 1993, ApJ, 415, L83
Smith, P. S., Balonek, T. J., Elston, R., & Heckert, P. A. 1987, ApJS, 64, 459
Stark, A. A., Gammie, C. F., Wilson, R. W., Bally, J., Linke, R. A., Heiles, C., & Hurwitz, M. 1992, ApJS, 79, 77
Steppe, H., Leichti, S., Mauersberger, R., Kompe, C., Brunswig, W., & Riuz-Moreno, M. 1992, A&AS, 96, 441
Steppe, H., Salter, C. J., Chini, R., Kraysa, E., Brunswig, W., & Lobato Perez, J. 1988, A&AS, 75, 317
Stickel, M., Fried, J. W., & Kühr, H. 1993, A&AS, 98, 393
Stickel, M., Padovani, P., Urry, C. M., Fried, J. W., & Kühr, H. 1991, ApJ, 374, 431
Stocke, J. T., et al. 1991, ApJS, 76, 813
Stocke, J. T., Liebert, J., Schmidt, G., Gioia, I. M., Maccacaro, T., Schild, R. E., Maccagni, D., & Arp, H. C. 1985, ApJ, 298, 619
Takalo, L. O. 1991, A&AS, 90, 161
Takalo, L. O., Kidger, M., de Diego, J. A., Sillanpää, A., Piirola, V., & Terasranta, H. 1990, A&AS, 83, 459
Takalo, L. O., Sillanpää, A., Nilsson, K., Kidger, M. R., De Diego, J. A., & Piirola, V. 1992, A&AS, 94, 37
Tanzi, E. G., et al. 1986, ApJ, 311, 13
Thompson, D. J., et al. 1993a, ApJ, 410, 87
Thompson, D. J., et al. 1993b, ApJ, 415, L13
Thompson, D. J., et al. 1995, ApJS, 101, 259
Treves, A., Belloni, T., Falomo, R., Fink, H., Maraschi, L., Sambruna, R. M., Tagliaferri, G., & Zimmermann, H. U. 1993, ApJ, 406, 447
Tucker, W. H. 1973, in Radiation Processes in Astrophysics (Cambridge, Mass.: MIT Press)
Ulvestad, J. S., & Johnston, K. J. 1984, AJ, 89, 189
Urry, C. M., et al. 1996, ApJ, 463, 424
Urry, C. M., & Padovani, P. 1995, PASP, 107, 803
Urry, C. M., Padovani, P., & Stickel, M. 1991, ApJ, 382, 501
Vagnetti, F., Giallongo, E., & Cavaliere, A. 1991, ApJ, 368, 366
Valtaoja, L., Karttunen, H., Valtaoja, E., Shakhovskoy, N. M., & Efimov, Y. 1993, A&A, 273, 393
Valtaoja, L., Valtaoja, E., Shakhovskoy, N. M., Efimov, Y. S., & Sillanpää, A. 1991, AJ, 101, 78
van Bruegel, W., & Schilizzi, R. 1986, ApJ, 301, 834
van Bruegel, W. J. M., Schilizzi, R. T., Hummel, E., & Kapahi, V. K. 1981, A&A, 96, 310
Vermeulen, R. C., & Cohen, M. H. 1994, ApJ, 430, 467
Véron-Cetty, M.-P., & Véron, P. 1993, A Catalogue of Quasars and Active Nuclei (ESO Sci. Rept. 13)
von Montigny, C., et al. 1995, ApJ, 440, 525
Wall, J. V., Danziger, I. J., Pettini, M., Warwick, R. S., & Wamsteker, W. 1986, MNRAS, 219, 23P
Wall, J. V., & Peacock, J. A. 1985, MNRAS, 216, 173
Webb, J. R., Smith, A. G., Leacock, R. J., Fitzgibbons, G. L., Gombola, P. P., & Shepherd, D. W. 1988, AJ, 95, 374
Weiler, K. W. & Johnston, K. J. 1980, MNRAS, 190, 269
Weistrop, D., Shaffer, D. B., Hintzen, P., & Romanishin, W. 1985, ApJ, 292, 614
Wills, B. J., Wills, D., Breger, M., Antonucci, R. R. J., & Barvainis, R. 1992, ApJ, 398, 454
Wolter, A., et al. 1991, ApJ, 369, 314
Worrall, D. M., et al. 1984a, ApJ, 284, 512
Worrall, D. M. et al. 1984b, ApJ, 278, 521
Wright, A., Ables, J. G., & Allen, D. A. 1983, MNRAS, 205, 793
Xie, G., et al. 1991, A&AS, 87, 461
Xie, G. Z., Li, K. H., Cheng, F. Z., Hao, P. J., Li, Z. L., Lu, R. W., & Li, G. H. 1990, A&A, 229, 329
Xie, G., et al. 1988a, AJ, 96, 24
Xie, G., et al. 1988b, A&AS, 72, 163
Xie, G., et al. 1987, A&AS, 67, 17
Zensus, J. A., Porcas, R. W., & Pauliny-Toth, I. I. K. 1984, A&A, 133, 27